Structure and Processing Relations in Ni-W Amorphous Particle Strengthened Ni Matrix Composites

Andrew Zeagler

Thesis submitted to the faculty of the
Virginia Polytechnic Institute and State University
in partial fulfillment of the requirements for the degree of

Master of Science
in
Materials Science and Engineering

Alex Aning, Chair
William Reynolds
Jeffrey Schultz

September 26, 2008
Blacksburg, VA

Keywords: Metal Matrix Composites, Amorphous, Particulate Reinforcement, Mechanical Alloying

Structure and Processing Relations in Ni-W Amorphous Particle Strengthened Ni Matrix Composites

Andrew Zeagler

ABSTRACT

Reinforcing metals with compositionally similar amorphous particles has been found to create composites with good interfacial bonding. It is conceivable that significant additional strengthening in amorphous reinforced composites can be realized by creating high-aspect ratio reinforcements; attritor milling holds promise in this regard. In this work, mechanical alloying was used to produce equimolar Ni-W powder that became a composite of amorphous Ni-W with undissolved W crystallites. A mixture of nickel powder and ten volume percent amorphous Ni-W powder was blended by attritor milling for either one or three hours, compacted by combustion-driven compaction and sintered for up to fifty hours at 600ºC. Prolonged times at elevated temperatures led to crystallization of the amorphous reinforcement particles and dissolution of tungsten into the matrix. Vickers macrohardness tests on the sintered composites yielded lower-than-expected values. Microscopy after hardness testing revealed sliding of particles at their boundaries, indicating poor bonding between them. It is believed that the sintering process was compromised by contamination from organic vapor present in the tube furnace used. While attritor milling effected smaller reinforcement particles, the small increase in aspect ratio likely would have been insufficient to cause significant strengthening by shear load transfer.

Acknowledgments

This work could not have been completed without the assistance of a number of individuals. David Berry always found time to show me how to use unfamiliar pieces of equipment. Niven Monsegue was patient in teaching me the intricacies of the attritor. Steve McCartney “drove” the SEM for me. Dr. Karthik Nagarathnam at UTRON, Inc., stepped up to compact my samples when HIPping fell through.

On the assessment side, Dr. Alex Aning, Dr. Bill Reynolds and Dr. Jeff Schulz graciously served on my committee and held me to rigorous standards.

To these people I would like to say thank you:

Thank you.

Table of Contents

1. Introduction 1
2. Background 3
2.1 Metal Matrix Composites 3
2.2 Mechanical Alloying 5
2.3 Amorphization of Metals 9
2.3.1 Amorphization by Rapid Solidification 9
2.3.2 Solid State Amorphization 9
2.3.3 Amorphization by Mechanical Alloying 10
2.4 Amorphous Reinforced Metal Matrix Composites 12
2.4.1 Consolidation by Combustion-Driven Compaction 13
2.5 Ni-W System 13
2.6 Nickel alloys 14
3. Experimental Procedure 15
3.1 Production of the Reinforcement Particles 15
3.2 Thermal Analysis of SPEX-Milled Powders 16
3.3 Production of the Composite Powder 16
3.4 Densification of Composite Powders 16
3.5 Analysis of Compacted Samples 17
4. Results and Discussion 18
4.1 Analysis of Particulate Reinforcements 18
4.1.1 X-ray Diffraction 18
4.1.2 Crystallite Size Analysis 19
4.1.3 Differential Scanning Calorimetry Analysis 20
4.2 Analysis of Composite Materials 21
4.2.1 Particle Size Analysis 21
4.2.2 Density 22
4.2.3 Microscopy 22
4.2.4 Vickers Hardness 45
5. Strengthening Model 46
5.1 Boundary Strengthening 46
5.2 Orowan Strengthening 47
5.3 Solid Solution Strengthening 49
5.4 The Effect of Aspect Ratio on Strengthening 49
5.5 Comment on Results 51
6. Summary 55
7. References 56
Appendix A: Image Analysis 61
Appendix B: Vickers macrohardness data 63
Appendix C: EDS data 64

List of Figures

Figure 1. Schematic of composite strengthening as a function of reinforcement diameter, aspect ratio, and volume fraction. 4
Figure 2. SPEX 8000 shaker mill and grinding vial with grinding media. 6
Figure 3. Diagram of the components of the stationary tank of an attritor mill. 6
Figure 4. Particle evolution during mechanical alloying. 8
Figure 5. (a) Hypothetical binary phase diagram showing the presence of an intermetallic phase. (b) Gibbs free energy versus composition at a temperature corresponding to Tr in the above diagram. 11
Figure 6. X-ray diffraction analysis of Ni-W powder after various milling times. 19
Figure 7. DSC analysis of Ni-W powder SPEX milled for 60 hours. 21
Figure 8. Photomicrograph of Ni with 10v.% Ni-W powder particles that have been attritor milled for 1 hour. 24
Figure 9. Photomicrograph of Ni with 10v.% Ni-W powder particles that have been attritor milled for 3 hours. 24
Figure 10. Photomicrograph of as-compacted Ni with 10v.% Ni-W after being attritor milled for 1 hour. 28
Figure 11. Photomicrograph of as-compacted Ni with 10v.% Ni-W after being attritor milled for 3 hours. 28
Figure 12. Photomicrograph of a composite of Ni with 10v.% Ni-W after being attritor milled for 1 hour and sintered for 5 hours.. 29
Figure 13. Photomicrograph of a composite of Ni with 10v.% Ni-W after being attritor milled for 1 hour, sintered for 5 hours and etched. 29
Figure 14. Photomicrograph of a composite of Ni with 10v.% Ni-W after being attritor milled for 1 hour and sintered for 10 hours. 30
Figure 15. Photomicrograph of a composite of Ni with 10v.% Ni-W after being attritor milled for 1 hour, sintered for 10 hours and etched. 30
Figure 16. Photomicrograph of a composite of Ni with 10v.% Ni-W after being attritor milled for 1 hour and sintered for 20 hours. 31
Figure 17. Photomicrograph of a composite of Ni with 10v.% Ni-W after being attritor milled for 1 hour, sintered for 20 hours and etched. 31
Figure 18. Photomicrograph of a composite of Ni with 10v.% Ni-W after being attritor milled for 1 hour and sintered for 30 hours. 32
Figure 19. Photomicrograph of a composite of Ni with 10v.% Ni-W after being attritor milled for 1 hour, sintered for 30 hours and etched. 32
Figure 20. Photomicrograph of a composite of Ni with 10v.% Ni-W after being attritor milled for 1 hour and sintered for 50 hours. 33
Figure 21. Photomicrograph of a composite of Ni with 10v.% Ni-W after being attritor milled for 1 hour, sintered for 50 hours and etched. 33
Figure 22. Photomicrograph of a composite of Ni with 10v.% Ni-W after being attritor milled for 3 hours and sintered for 5 hours. 34
Figure 23. Photomicrograph of a composite of Ni with 10v.% Ni-W after being attritor milled for 3 hours and sintered for 10 hours. 35

Figure 24. Photomicrograph of a composite of Ni with 10v.% Ni-W after being attritor milled for 3 hours, sintered for 10 hours and etched. 35
Figure 25. Photomicrograph of a composite of Ni with 10v.% Ni-W after being attritor milled for 3 hours and sintered for 20 hours. 36
Figure 26. Photomicrograph of a composite of Ni with 10v.% Ni-W after being attritor milled for 3 hours, sintered for 20 hours and etched. 36
Figure 27. Photomicrograph of a composite of Ni with 10v.% Ni-W after being attritor milled for 3 hours and sintered for 30 hours. 37
Figure 28. Photomicrograph of a composite of Ni with 10v.% Ni-W after being attritor milled for 3 hours, sintered for 30 hours and etched. 37
Figure 29. Photomicrograph of a composite of Ni with 10v.% Ni-W after being attritor milled for 3 hours and sintered for 50 hours. 38
Figure 30. Photomicrograph of a composite of Ni with 10v.% Ni-W after being attritor milled for 3 hours, sintered for 50 hours and etched. 38
Figure 31. Scanning electron micrograph of a composite of Ni with 10v.% Ni-W after being attritor milled for 1 hour and sintered for 10 hours. 39
Figure 32. Scanning electron micrograph of a composite of Ni with 10v.% Ni-W after being attritor milled for 1 hour and sintered for 10 hours. 39
Figure 33. Scanning electron micrograph of a composite of Ni with 10v.% Ni-W after being attritor milled for 1 hour and sintered for 30 hours. 40
Figure 34. Scanning electron micrograph of a composite of Ni with 10v.% Ni-W after being attritor milled for 1 hour and sintered for 30 hours. 40
Figure 35. Scanning electron micrograph of a composite of Ni with 10v.% Ni-W after being attritor milled for 1 hour and sintered for 50 hours. 41
Figure 36. Scanning electron micrograph of a composite of Ni with 10v.% Ni-W after being attritor milled for 1 hour and sintered for 50 hours. 41
Figure 37. Scanning electron micrograph of a composite of Ni with 10v.% Ni-W after being attritor milled for 3 hours and sintered for 10 hours. 42
Figure 38. Scanning electron micrograph of a composite of Ni with 10v.% Ni-W after being attritor milled for 3 hours and sintered for 10 hours. 42
Figure 39. Scanning electron micrograph of a composite of Ni with 10v.% Ni-W after being attritor milled for 3 hours and sintered for 30 hours. 43
Figure 40. Scanning electron micrograph of a composite of Ni with 10v.% Ni-W after being attritor milled for 3 hours and sintered for 30 hours. 43
Figure 41. Scanning electron micrograph of a composite of Ni with 10v.% Ni-W after being attritor milled for 3 hours and sintered for 50 hours. 44
Figure 42. Scanning electron micrograph of a composite of Ni with 10v.% Ni-W after being attritor milled for 3 hours and sintered for 50 hours. 44
Figure 44. Photomicrograph of a composite of Ni with 10v.% Ni-W after being attritor milled for 3 hours and sintered for 5 hours 45
Figure 45. Plot of predicted strengthening contributions in the samples attritor-milled for one hour. 52
Figure 46. Plot of predicted strengthening contributions in the samples attritor-milled for three hour. 53
Figure 47. Plot of predicted strengthening contributions in the two attritor-milled samples. 54

List of Tables

Table 1. Calculations of tungsten crystallite size from X-ray diffraction peaks of SPEX-milled powder samples.....20
Table 2. Calculations of reinforcement aspect ratios through SEM image analysis in ImageJ. 25
Table 3. The expected increase in tensile strength due to boundary strengthening calculated for each attritor milling time/sintering time combination. 47
Table 4. The expected increase in tensile strength due to Orowan strengthening calculated for each attritor milling time/sintering time combination. 48
Table 5. The expected increase in shear strength due to solid solution strengthening calculated for each attritor milling time/sintering time combination. 50

1. Introduction

It has long been known that materials composed of more than one phase can exhibit mechanical properties that surpass those of the constituent phases. In metals, multi-phase materials traditionally have been realized through alloying and heat treating. More recently, however, metals have been combined in a composite (i.e. a combination of two components separated by a distinct interface, thermodynamically irreversible, and has properties that can be engineered using composite principles [1]).

A common objective in creating a metal matrix composite is to increase the strength without sacrificing too much ductility, as compared to the main constituent material. The interfaces between constituents play a large role here, transferring loads and impeding dislocation motion. Accordingly, it is important to consider the interfacial bonding when forming a composite. A metal and ceramic, for example, may not bond as well as two metals; in a worst case scenario, the two constituents debond completely and the reinforcement particles essentially function as voids.

Employment of an amorphous metal as the reinforcement is one way to avoid problems with bonding, particularly when the two phases have similar composition. Amorphous metals typically exhibit high strength as compared to their crystalline counterparts, since they possess no dislocations to facilitate plastic deformation. Amorphous metal reinforcements are not without their own set of disadvantages, however. The phase's metastability implies operational and processing limits (i.e. sufficiently high service/processing temperatures will lead to crystallization and therefore decreased strength). Also, the energy requirements of amorphization can make production expensive.

A number of techniques have proven successful in producing amorphous metals, including rapid quenching [2], irradiation [3, 4], solid-state amorphization reaction [5], and

mechanical alloying [6, 7]. Mechanical alloying, the technique employed in this study, is a powder processing technique that involves repeated fracturing and welding of the starting powders, and is chosen here because its ability to produce an amorphous alloy of the desired composition has been demonstrated [8].

Similarly, there are a number of options for consolidation of metal powders: cold pressing, liquid and solid-phase sintering, hot-uniaxial [9] and hot-isostatic pressing [10, 11], warm rolling [12], warm extrusion [13], shock compression [14-17], and spark plasma sintering [18, 19]. A new technique called combustion-driven compaction, which employs energy released during combustion of gases to compact powders into net-shaped parts, was used for this work.

In this study, equimolar nickel and tungsten powders were milled in a high-energy SPEX mill for sixty hours to induce amorphization. These powders were then blended with nickel to form a mixture of Ni + 10 v.% Ni-W. Prior to combustion-driven compaction, the mixture was blended in an attritor mill; subsequent to compaction, the compacted samples were sintered. Attritor milling and sintering times were varied so as to study how processing affects the structure and mechanical properties of the final composite.

2. Background

2.1 Metal Matrix Composites

Though the engineering of metal matrix composites is a fairly recent development, man has been making composites for quite some time. The ancient Egyptians were perhaps the first to engineer a composite material: they reinforced mud (clay and water) with straw to create adobe bricks [20]. Nature also generates its own composites. For example, wood is a combination of cellulose fiber and lignin; the cellulose fiber provides strength and the lignin stabilizes the fibers. (Man, in turn, can make a composite out of this composite by combining wood veneer with an adhesive to form a laminated structure called plywood.)

Ductile iron, invented by Keith Millis in 1943, is an early example of a metal matrix composite, and is the result of a very specific casting process in which a magnesium treatment and a ferrosilicate inoculant promote the formation of spherical graphite particles [21]. Upon cooling, ferrite forms around the graphite and a matrix of pearlite nucleates and grows out of the remaining austenite. Ductile iron shows an improvement in ductility as compared to grey iron, as the graphite nodules do not provide a convenient path for crack propagation, unlike the graphite flakes in grey iron.

Wide-ranging research on dispersion strengthened alloys was conducted in the 1950s and 1960s, generally with a view towards increased strength [22]. In a dispersion strengthened alloy, the dispersoids (less than 1 μm in diameter) provide a non-coherent interface that impedes dislocation movement. Also contributing to strengthening is work hardening of the matrix due to Orowan looping [23]. With increasing dispersoid size, assuming constant volume fraction of reinforcement, comes increased interparticle spacing. In this case, dislocations are freer to move and less strengthening is achieved.

This relationship between particle size and strengthening is shown in the left diagram in Figure 1.

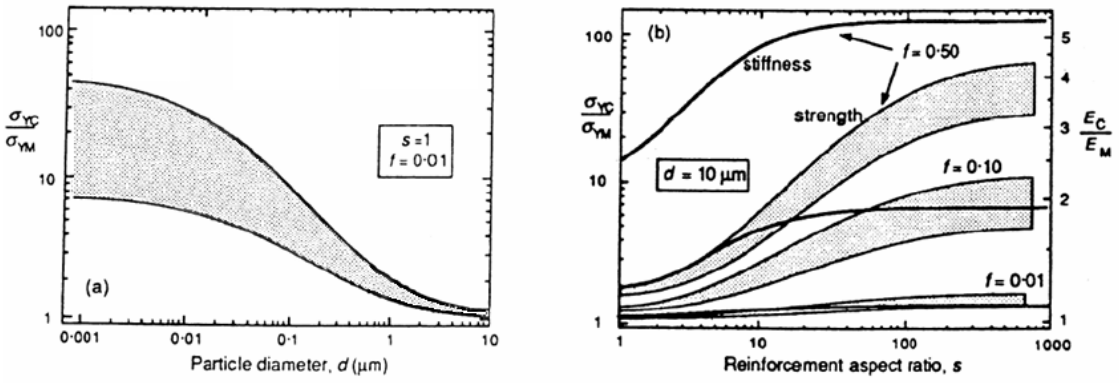

Figure 1. Schematic of composite strengthening as a function of reinforcement diameter (d), aspect ratio (s), and volume fraction (f). The left illustration shows matrix dominated strengthening. The right illustration shows stiffening and strengthening gained from load transfer to high aspect ration reinforcement. (Cambridge University Press grants permission freely for the reproduction in another work of a single figure in which it holds rights.) [22]

The next significant advancement in metal matrix composites emerged in the 1960s with the development of fiber reinforcements [22]. In these composites, transference of an applied load to the fibers is the chief function of the matrix; thus, good bonding between the two constituents is essential. The inconvenience of manufacturing continuous fiber reinforced composites, however, led to a shift towards discontinuous fiber reinforced composites in the 1980s [22]. Discontinuous fibers, sometimes called whiskers, are easier to manufacture and novel processing methods are not required to create the final composite (e.g. in a cast material, fibers can be introduced to the melt). As might be expected, the main strengthening mechanism in this material is dependent on the aspect ratio of the reinforcement. In high aspect ratio specimens, shear load transfer dominates and the behavior is like that of fiber reinforced composites; in low aspect ratio specimens, matrix strengthening dominates and the behavior is like that of dispersion

strengthened alloys. The relationship between reinforcement diameter and strengthening is shown in the right diagram in Figure 1.

Most recently, a process called mechanical alloying has been employed to create amorphous particles of similar chemistry to the matrix, which generally leads to good bonging between matrix and reinforcement [24, 25].

2.2 Mechanical Alloying

Mechanical alloying (MA) is a solid-state powder processing technique involving repeated welding, fracturing, and rewelding of powder particles, typically carried out in a high-energy ball mill. In a SPEX mill, the type used in this study, 10-20 grams of metal powders of known composition are loaded into a vial along with spherical grinding media and shaken in an approximate figure eight pattern at approximately 1200 hertz [26]. With a lateral motion of 5 cm, ball velocity, and consequently impact energy, is quite high. Examples of a SPEX mill, grinding vial and grinding media are shown in Figure 2. Available vial and grinding media materials include stainless steel, hardened steel and tungsten carbide; stainless steel was used for this work.

A few other types of mills have been developed for mechanical alloying. In a planetary ball mill, multiple vials are rotated not only around their own axis, but also around a parallel central axis. The vials and supporting disk rotate in opposite directions, causing both impact and friction effects as the balls collide with the vial wall and run down the side. In an attritor mill, a stationary upright drum is half-filled with grinding media and a rotating impeller agitates the media. (A diagram of the stationary tank is shown in Figure 3.) As the energy is imparted only by friction, attrition milling is a lower energy process than shaker or planetary milling. Larger mills exist for commercial

operation, some with different methods of operation, but the principle of imparting a large amount of energy through grinding media remains the same.

Figure 2. SPEX 8000 shaker mill (left) and grinding vial with grinding media (right). Reprinted from Suryanarayana, C., *Mechanical alloying and milling.* Progress in Materials Science, 2001. 46[**1-2]: p. 1-184.), with permission from Elsevier.**

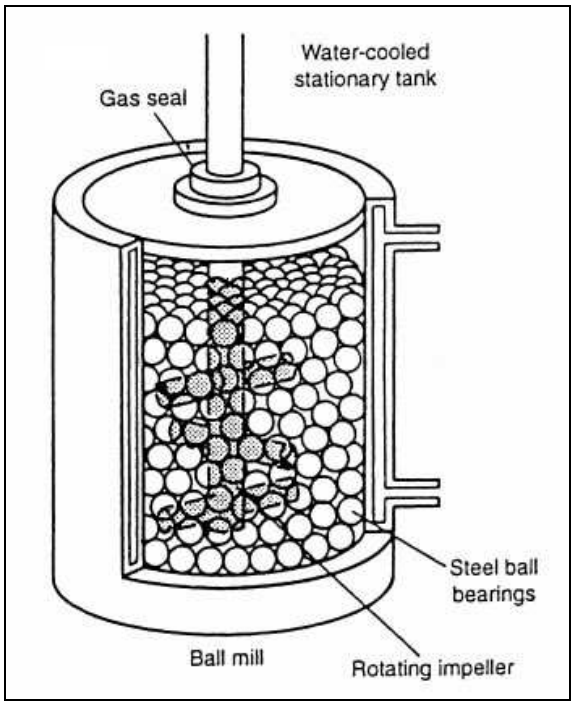

Figure 3. Diagram of the components of the stationary tank of an attritor mill. Reprinted from Suryanarayana, C., *Mechanical alloying and milling.* Progress in Materials Science, 2001. 46[**1-2]: p. 1-184.), with permission from Elsevier.**

Besides mill type, there are a number of process variables that can be controlled to optimize conditions for amorphization. The vial material and grinding media must be carefully chosen to avoid contaminating the powder. Milling speed can be varied with some mills, but excessively high temperatures need to be avoided so as not to provide adequate driving force for crystallization. Also, high milling speeds can pin the grinding media to the vial wall in some types of mills. The charge ratio, or the ratio of the weight of the balls to the powder, can be increased to shorten the amount of time required for amorphization, but this can also generate more heat. Milling atmosphere must also be chosen so as not to contaminate the powder.

Mechanical alloying was developed around 1966 at the International Nickel Company (INCO) by John Benjamin and colleagues [6, 7], who were attempting to produce a nickel-based superalloy that would combine the high-temperature strength of oxide dispersion and the intermediate-temperature strength of gamma-prime precipitate. Since then the technique has found application as a processing technique for numerous materials, including metals [27, 28], ceramics [29, 30], polymers [31, 32] and their mixtures [33, 34].

A number of phenomena have been observed through mechanical alloying that are sometimes more difficult, or even impossible, to achieve via other methods. Rapid solidification processing [35] and vapor deposition [36] have previously been shown to achieve extensions in solid solubility for many alloy systems, and now there is a growing list of alloy systems for which solid solubility can be extended through MA [26]. Similarly, MA can produce a large number of intermetallics, many of which are metastable and cannot be realized through traditional casting/heat treating methods [26]. Iron and copper, for example, segregate upon cooling from a melt, but this can be circumvented by MA [37]. (MA can also produce intermetallics that are uneconomical to

cast due to a high melting temperature of one component.) MA has even been shown to induce chemical reactions in certain metal or ceramic systems [26]. But most importantly for this work, MA is adept at creating amorphous alloys, which previously could only be formed by rapid solidification. The amorphization of metals will be discussed further in the next section.

Repeating processes of fracture and welding occur during mechanical alloying and begin when powder particles become trapped between the grinding media. The impact causes the particles to plastically deform, leading to work hardening and fracture. Cold welding then takes place between newly revealed surfaces, forming a lamellar structure. Under continued impact events, the structure of the powder particles refines until individual lamellae are no longer resolvable with an optical microscope. Eventually, the process will reach a steady state where the rate of welding and the rate of fracture make for an unchanging, narrow particle size range [38]. All the while, amorphization takes place near the interfaces between the two constituents. (Various stages of the mechanical alloying process are shown in Figure 4.)

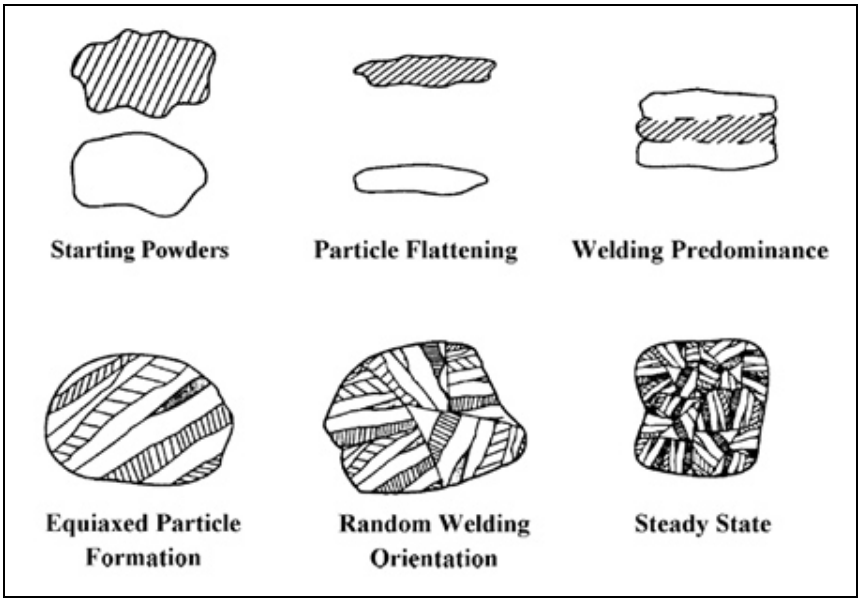

Figure 4. Particle evolution during mechanical alloying. [39] With kind permission of Springer Science and Business Media.

2.3 Amorphization of Metals

2.3.1 Amorphization by Rapid Solidification

As amorphous materials by definition lack an ordered atomic arrangement, and metals are in their lowest room temperature energy state when crystalline, formation of an amorphous metal involves controlling kinetics such that atoms cannot rearrange into an ordered structure. This was first achieved in 1960 by Klement et. at., who propelled a liquid metal droplet onto a cooled metal surface and found cooling rates of 10^6 K/min., which was sufficient to form a thin foil of amorphous metal [2]. Further research led to successful production of a number of amorphous alloys, most of which were found to have mechanical properties that exceeded those of their crystalline counterparts [40].

Turnbull later showed that metals have glass transition temperatures and published a criterion for glass formability in metals: $T_g/T_m = 2/3$, where T_g and T_m are the glass transition temperature (i.e. the temperature above which viscous flow occurs in an amorphous solid) and melting temperature, respectively [41]. One important limitation, however, was that the composition of the alloy must be near a deep eutectic. Subsequent research took advantage of these criteria to find materials systems that would form metallic glasses at lower cooling rates [42].

2.3.2 Solid State Amorphization

There are a number of techniques capable of producing amorphous metals without melting the constituents; these are collectively termed solid state amorphization reactions (SSARs). Irradiation, hydrogen diffusion, diffusion-induced amorphization in multilayers and mechanical alloying are a few examples of SSARs. With irradiation, the

goal is to devastate the crystal lattice through the creation of defects. This is accomplished by bombarding the material with fast-moving high energy particles [43]. Hydrogen amorphization was first observed in lanthanum-nickel alloys in 1976 [44], leading to further studies in the 1980s in which crystalline-to-amorphous transitions were shown in a number of alloys containing the Laves phases of nickel and rare earth metals [45].

Similar studies in which hydrogen was replaced by a metal were conducted by Schwarz et. al., who determined that two criteria must be met for solid state amorphization to take place in metallic couples:

1. The heat of mixing between the two species must be large and negative
2. One specie must diffuse anomalously fast into the other

Heat of mixing is the difference between the enthalpy of the mixture and the sum of the constituent enthalpies (at the same temperature and pressure). A large negative heat of mixing provides thermodynamic driving force for diffusion, while the difference in diffusion rates prevents the formation of an intermetallic [5]. Examples of materials systems that meet these criteria and have been shown to amorphize by SSAR include Ni-Ti [46], Cu-Ti [47] and Co-Ti [48].

2.3.3 Amorphization by Mechanical Alloying

Since mechanical alloying work hardens each constituent lattice and causes the formation of thin lamellae, mechanical alloying can be considered a large-scale method of diffusion-induced amorphization in multilayers. Equiatomic compositions are most favorable for amorphization by MA [49], unlike rapid solidification, for which amorphization is most likely at compositions near a eutectic. This is illustrated in the hypothetical binary phase diagram in the upper plot of Figure 5. Here α and β are the terminal solid solutions, γ is an intermetallic and L is the liquid phase; the Gibbs free

energy of these phases at temperature T_r is shown as a function of composition in the lower plot. (It is assumed that the Gibbs free energy of the amorphous phase is equivalent to that of the liquid.) Only α, β and γ (or combinations thereof) are stable at this temperature, while the amorphous phase is metastable. For an equiatomic composition, MA essentially creates a blended elemental powder mixture with Gibbs free energy corresponding to point 1 on the lower plot. Thus formation of the amorphous phase is energetically favorable, though less favorable than the intermetallic.

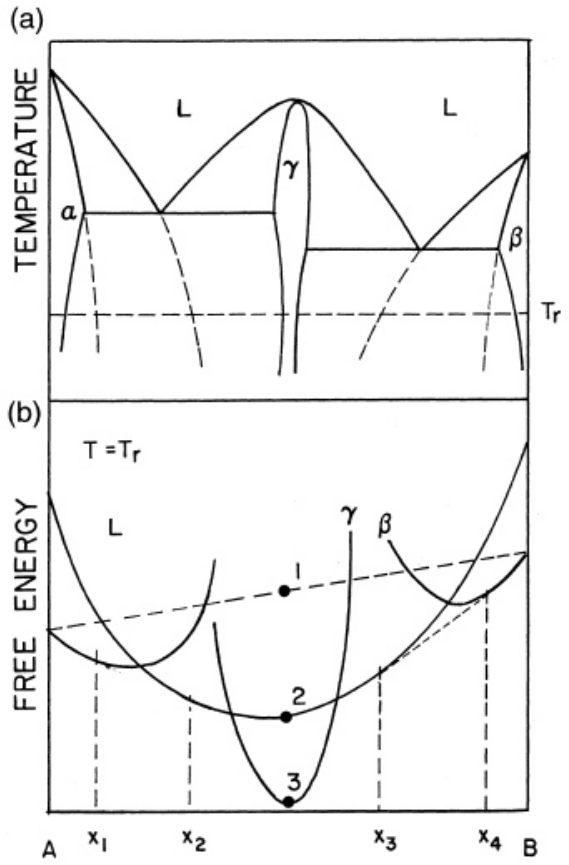

Figure 5. (a) Hypothetical binary phase diagram showing the presence of an intermetallic phase. (b) Gibbs free energy versus composition at a temperature corresponding to T_r in the above diagram. Reprinted from Suryanarayana, C., *Mechanical alloying and milling.* Progress in Materials Science, 2001. 46**[1-2]: p. 1-184.), with permission from Elsevier.**

The criteria put forth in the previous section were initially speculated to be applicable for MA [50], and numerous materials systems that meet these criteria have indeed been shown to amorphize by MA, such as Ni-Zr [51], Cu-Zr [52], Ni-Ti [53] and Cu-Hf [54]. On the other hand, the materials system that is the focus of this study, Ni-W, is an exception. It has been shown to amorphize though the heat of mixing magnitude is very small [8]. In the absence of this driving force, amorphization takes place only when MA has forced a local composition of 28 at. % W.

2.4 Amorphous Reinforced Metal Matrix Composites

The use of amorphous metals as reinforcement is a recent development in materials science. In some of the earliest work, performed in the mid-1970s, resin matrices were reinforced with amorphous metal ribbons. Shear strengths were lower than predicted, however, and it was shown that the resin did not adhere to the smooth side of the ribbon [55]. Later, vacuum hot pressing was demonstrated to form a good bond between $Ni_{60}Nb_{40}$ amorphous ribbons and a superplastic aluminum alloy in work published by Cytron [56].

Blank-Bewersdorf reinforced a Ni matrix with amorphous $Fe_{42}Ni_{42}B_{16}$ and found improved interfacial strength after a short heat treatment [57]. This extra step brought about some crystallization at the interface and led to improved bonding. Most recently, Zhang et. al. synthesized amorphous Al-Ni-La particles in an aluminum matrix by in-situ devitrification [58]. They found uniformly distributed particles that were bonded well to the matrix. Mechanical properties exhibited a good balance between strength and ductility; high thermal stability was also observed.

2.4.1 Consolidation by Combustion-Driven Compaction

Developed by UTRON, Inc., combustion-driven compaction is a novel processing method that takes advantage of energy released during combustion of gases to compact powders into net-shaped powder metallurgy parts. After the powder is loaded, natural gas and air fills a chamber to high pressure, which cause initial powder compaction as the piston is forced out of the chamber. Then the gas supply is closed and the gas in the chamber ignited, which triggers a dramatic rise in pressure that further drives the piston, compressing the powder into its final shape. Pressures between 50 and 150 tsi can be achieved, though the loading rate is gentle enough to avoid shock propagation [59].

Though the technology is recent, potential applications are emerging. CDC has already been shown to hold promise for making permanent magnets [60]. UTRON's own work has demonstrated mechanical properties in sintered CDC Al-Mg alloys that are comparable to those attained by annealing [59].

2.5 Ni-W System

The nickel-tungsten system has undergone limited research as a possible reinforcement in metal matrix composites. The formation of amorphous Ni-W has been shown possible by electrodeposition [61-63]. Aning et. al. synthesized amorphous Ni-W by mechanical alloying and determined the tungsten content in the nickel phase must exceed 28 at. % in order for amorphization to proceed. They also showed Fe contamination resulting from grinding media wear during milling of Ni-W powder blends plays only a minor role in solution and amorphization kinetics [8]. Mukira and Courtney studied consolidation and crystallization behavior of amorphous Ni-W powder blends

produced via MA and discovered that three phases evolve during heat treatment: W, (Ni-Fe)W intermetallic, and Ni-rich FCC [64].

2.6 Nickel alloys

As the composites in this study would be candidates for replacing current nickel alloying, it is valuable to survey the current state of nickel alloys.

Commercially pure nickel typically contains up to 1 percent residual content in the form of solute atoms of copper, iron, carbon, manganese and/or silicon. Room temperature tensile strength of pure nickel ranges from 400–460 MPa, but falls to 176 MPa at 600ºC [65]. A modified version of Alloy 400 (65% Ni, 35% Cu), called K-500, includes 2.5% Al and 0.5% Ti for the purpose of precipitation hardening. Tensile strength in this alloy exceeds 1 GPa, and it finds application where good corrosion resistance is a requirement [66].

A number of nickel superalloys have been developed in recent years, offering high strengths and corrosion resistance at elevated temperatures. ASM Handbook, Vol. 1, lists a number of nickel-base alloys with tensile strengths that exceed 1 GPa and a few with yield strengths in the GPa range, as well. Yield strengths at 537ºC often exceed 800 MPa; data are scarcer at 1093ºC, but a few alloys have demonstrated yield strengths that range from 200–500 MPa [67].

3. Experimental Procedure

3.1 Production of the Reinforcement Particles

The composition of the amorphous reinforcement was chosen to be Ni – 50 at. % W. To minimize oxide content, the as-received -325 mesh nickel and -325 mesh tungsten powders were reduced in a hydrogen atmosphere at 500ºC for one hour in a Lindberg/Bluem tube furnace. For the same reason, the powders were stored and milled in an argon atmosphere. Milling was carried out in a SPEX Mixer/Mill 8000D with stainless steel vials (SPEX 8007) and 7/16" diameter stainless steel balls (Winsted Precision Ball Company 440C). In each cycle, 11.90 grams of equiatomic Ni-W powder was loaded into the vial along with eleven stainless steel balls for a charge ratio of 6:1. (Charge ratio is defined as the ratio of grinding media mass to powder mass.) The mill was run for sixty hours, but interrupted after one, three, five and ten hours for the purpose of flipping and rotating the vial to avoid powder accumulation in dead zones. The material requirements of the compaction step necessitated that multiple batches of powder be amorphized in the SPEX mill.

X-ray diffraction analysis of the final, as well as starting and intermediate, powders was performed using a PANalyitcal X'Pert PRO X-ray diffractometer system. This machine used a copper source for X-rays with a generator power of 45 kV and 40 mA. Scans were performed using fixed slits (0.04 rads) and an incident scatter slit of 1 degree. The sample stage rotated at a speed of one revolution per second.

3.2 Thermal Analysis of SPEX-Milled Powders

Differential scanning calorimetry (DSC) was performed on the sixty-hour SPEX-milled powder sample using a Netzsch STA 449 C Jupiter TG-DSC. The sample was contained in an alumina crucible and the chamber then sealed and purged twice with helium. Then the sample was heated from 25ºC to 1200ºC at 20.0 K/min, and observed peaks were analyzed using the Proteus software.

3.3 Production of the Composite Powder

A composition of 10 volume percent amorphous reinforcement in a pure nickel matrix was chosen for this study. A Szegvari Attritor mill was used to blend the reinforcing and matrix powders, with 3/8" diameter stainless steel balls as the grinding media. The charge ratio was maintained at 32:1, and the impeller at 400 rpm. Argon was fed through the mixing drum to minimize oxidation, and a water jacket cooled the drum so as to avoid crystallization of the amorphous phase. Separate runs of one and three hours were performed.

3.4 Densification of Composite Powders

Densification of the composite powders was achieved using combustion-driven compaction (CDC), which was performed by Dr. Karthik Nagarathnam at UTRON, Inc. in Manassas, Virginia. Approximately 20 grams of composite powder were compacted into a disk 1" in diameter and 11/64" in thickness. One disk was compacted for each composite sample (one- and three-hour attritor-blended Ni + 10 vol. % Ni-W). Small bars were then cut from each disk using a Struers Accutom-5 with a diamond wheel.

Sintering was then performed in a Lindberg/Bluem tube furnace; for each sample, specimens were sintered in hydrogen at 600ºC for 5, 10, 20, 30 and 50 hours.

3.5 Analysis of Compacted Samples

A number of techniques were employed to analyze the compacted composite samples, including optical microscopy, scanning electron microscopy (SEM), energy dispersive X-ray analysis (EDS) and Vickers macrohardness testing.

Preparation for optical and scanning electron microscopy entailed mounting samples in bakelite, a thermosetting polymer. These mounts were then ground and polished with alumina powder in a number of steps (down to 0.05 μm alumina). Optical micrographs were taken of each sample using a Carl Zeiss Axiovert 200M microscope.

SEM was performed on a FEI Quanta 600 FEG using the same samples as with optical microscopy, except a 10 nm coating of gold was sputtered onto the samples to conduct charge away from the surface during examination. EDS maps were generated for areas that coincide with selected SEM images.

Vickers macrohardness tests were performed using a Leco LV700 AT; a 10 kg load was applied for ten seconds.

4. Results and Discussion

4.1 Analysis of Particulate Reinforcements

4.1.1 X-ray Diffraction

X-ray diffraction was performed on the Ni-W powder mixture at three stages: unmilled and after ten and sixty hours of milling. While more steps would have presented a clearer trend concerning the microstructural evolution of Ni-W during mechanical alloying, such work has already been performed by Aning et. al. [8]. Figure 6 shows prominent nickel and tungsten peaks in the unmilled sample, as expected. After ten hours of milling, characteristic tungsten peaks show a decrease in intensity as compared with the unmilled sample. In the place of nickel peaks, a broad peak forms that is centered on an angle slightly smaller than that of dominant nickel peak in the unmilled sample – in X-ray diffraction, this is the distinguishing feature of an amorphous material. The angle of the peak indicates there has been significant diffusion of larger tungsten atoms into areas of nickel. The broadness of the peak points toward an amorphous structure, for which the wide range of bond lengths will cause some diffraction at a similarly wide range of angles. Due to limitations on the amount of tungsten that can dissolve into the amorphous Ni-W phase during mechanical alloying, some regions of high tungsten concentration will remain in the powder particles. These regions are manifested in the X-ray diffraction plot as smaller peaks that are shifted to slightly greater angles as compared with the unmilled sample. These tungsten peaks are also broader, suggesting that small crystallites remain.

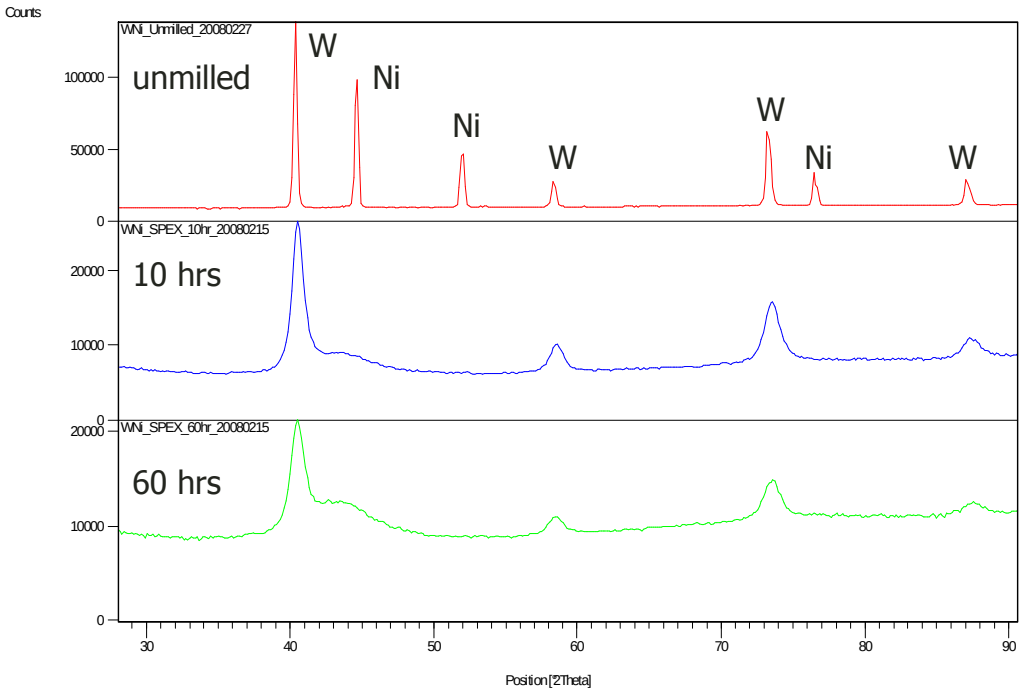

Figure 6. X-ray diffraction analysis of Ni-W powder after various milling times. All peaks show a substantial drop in intensity, and nickel peaks broaden considerably; both events are indicative of amorphization.

4.1.2 Crystallite Size Analysis

It was speculated that the remaining tungsten peaks indicated the presence of tiny particles within the amorphous Ni-W. Calculation of the size of crystallites within the particles was done using the Scherrer formula, which has the relation

$$t = \frac{0.9\lambda}{B\cos\theta_B} \qquad (1)$$

where t is the crystallite size, λ is the X-ray wavelength, B is the full width at half the maximum intensity of a diffraction peak and θ_B is the peak diffraction angle in radians. Table 1 shows the results of these calculations.

Unmilled

Peak FWHM (degrees)	Peak Position (degrees)	Crystallite size (nm)
0.25	40.4	35
0.55	58.4	17
0.60	73.3	17
0.70	87.1	16

SPEX 10 hr

Peak FWHM (degrees)	Peak Position (degrees)	Crystallite size (nm)
1.1	40.7	8.1
1.2	58.7	7.9
1.4	73.5	7.4
1.6	87.5	7.2

SPEX 60 hr

Peak FWHM (degrees)	Peak Position (degrees)	Crystallite size (nm)
1.5	40.6	5.9
1.5	58.5	6.3
1.6	73.5	6.5
1.9	87.5	6.1

Table 1. Calculations of tungsten crystallite size from X-ray diffraction peaks of SPEX-milled powder samples. Small crystallites are already present in the unmilled powder; ten hours of SPEX-milling more than halves their diameter, but the returns have diminished by sixty hours.

4.1.3 Differential Scanning Calorimetry Analysis

Differential scanning calorimetry (DSC) was used to determine the temperature at which the amorphous Ni-W phase crystallizes, for the purpose of establishing heat treatment and operational temperature limits. The resulting plot is shown in Figure 7. Heat flux increases linearly to a temperature of approximately 540ºC, where there is a possible glass transition peak, then continues increasing linearly until crystallization occurs. Using the Proteus software, it was determined that the peak corresponding with crystallization lies at 742.2ºC, with the onset at 728.7ºC.

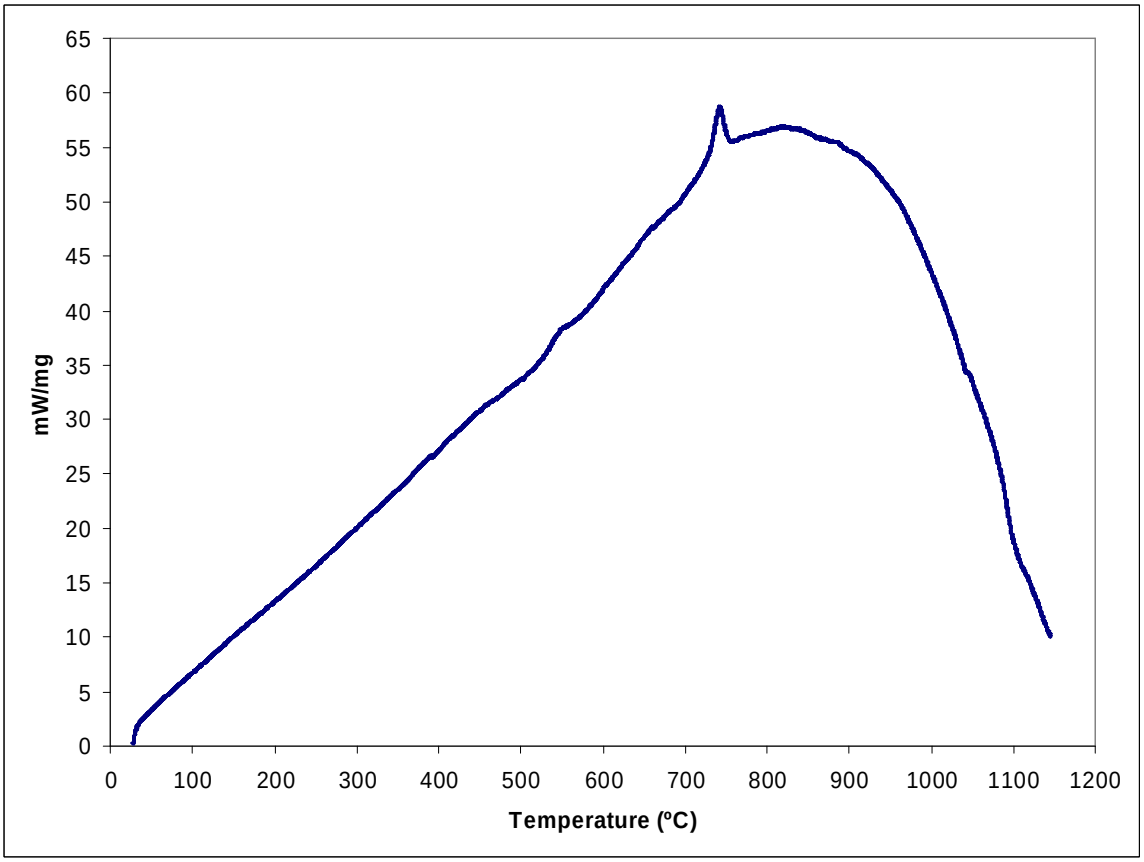

Figure 7. DSC analysis of Ni-W powder SPEX milled for 60 hours. An exothermic peak, corresponding to crystallization, is centered around 742ºC. The slight deviation from linearity near 540ºC may correspond to the glass transition temperature.

4.2 Analysis of Composite Materials

4.2.1 Particle Size Analysis

Prior to compaction, attritor-blended powders were analyzed. Image analysis of photomicrographs yielded average particle sizes of 57.2 μm and 249.4 μm for powders blended for one and three hours, respectively. The procedure is outlined and the raw data presented in Appendix A.

A Horiba particle size analyzer was also employed in an attempt to discern particle size. However, results were skewed due to poor wetting of the largest particles, which floated on the water. Thus, only the smaller particles were analyzed and the resulting values are not representative.

4.2.2 Density

The density of as-received compacted samples was calculated using Archimedes' principle. The composite that had been attritor milled for one hour was found to have a density of 8.35 g/cm^3, and the three hour sample 7.77 g/cm^3. In the three hour sample, the extra milling time allowed for extensive welding of the two constituents (an event infrequently observed in the one hour sample). The microstructure of individual powder particles was a microcosm of the final composite, where small reinforcement particles were embedded in a nickel matrix. These reinforced powder particles were less able to deform during compaction than the relatively pure nickel powder particles in the one hour sample, thus a lower density was calculated.

4.2.3 Microscopy

Optical and SEM micrographs of the material at various stages along the path to the final composite are shown in Figures 8 through 43. (All samples were mounted in Bakelite and polished with alumina powder.) Figure 8 and Figure 9 show the powder particles that result after the amorphous Ni-W powder was blended with Ni matrix powder in an attritor. The samples were etched with a solution of 0.5 g CrO_3 in 100 mL HCl to differentiate between the two constituents; here the lightest particles are amorphous Ni-W and the rest are Ni. In Figure 8, a significant fraction of the nickel

particles are elongated, while most of the Ni-W particles remain equiaxed. In Figure 9, however, the extra two hours of attritor milling have led to amorphous particles of decreased size and increased aspect ratio. Thus, it is expected that the strengthening mechanisms discussed in section 2.1 will play a role in the mechanical properties of the final composite.

Figure 10 and Figure 11 show massive porosity in the as-compacted composites, necessitating sintering to form a usable material.

Compacted, sintered samples were analyzed using optical microscopy and SEM; definitive identification of the microconstituents was facilitated by EDS. Figures 12 through 30 show optical micrographs of each sample, Figures 31 through 42 present SEM images of each sample and corresponding EDS maps for selected samples. In optical micrographs, the lightest areas are the most nickel-rich and the darkest areas are the most tungsten-rich; this is reversed in the SEM images. EDS maps display nickel as green and tungsten as red (see Appendix C).

The series of optical and SEM images of compacted samples show consistency in the size of the reinforcement particles with respect to sintering time, but not with respect to attrition time. Where the reinforcement was attritor milled for one hour, equiaxed reinforcement particles with a diameter around 25 μm are typical; after three hours of milling, however, reinforcement particles are generally ellipsoidal with a major axis that compares well with the diameters observed after one hour of milling. Minor axes, however, were appreciably smaller. (The difference in particle morphology is of course attributable to the attritor milling process, in which the repeated welding, deformation and fracture of the reinforcement and matrix particles occurs.) Using a freeware image analysis program, aspect ratios of the reinforcement particles were calculated. Average values, shown in Table 2, were greater in the samples attritor milled for three hours, but the values are not large enough that substantial strengthening by load transfer is to be expected.

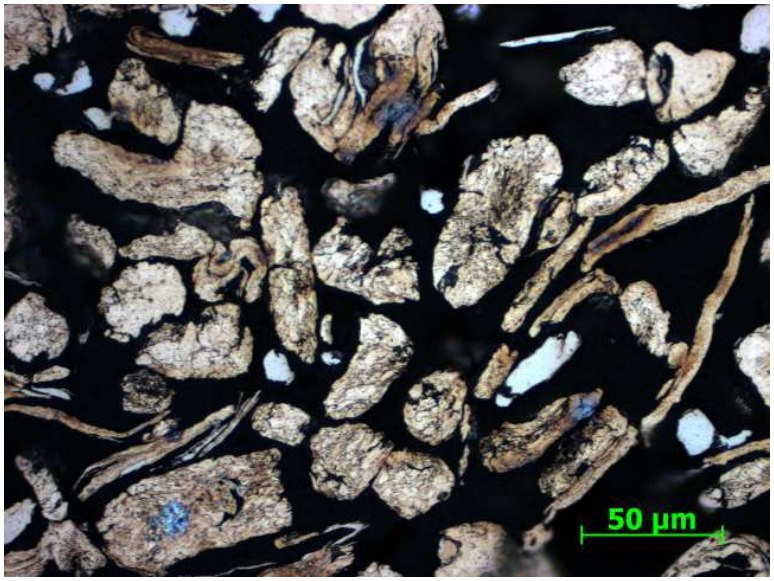

Figure 8. Photomicrograph of Ni with 10v.% Ni-W powder particles that have been attritor milled for 1 hour. The lightest particles, most of which remained equiaxed, are amorphous Ni-W.

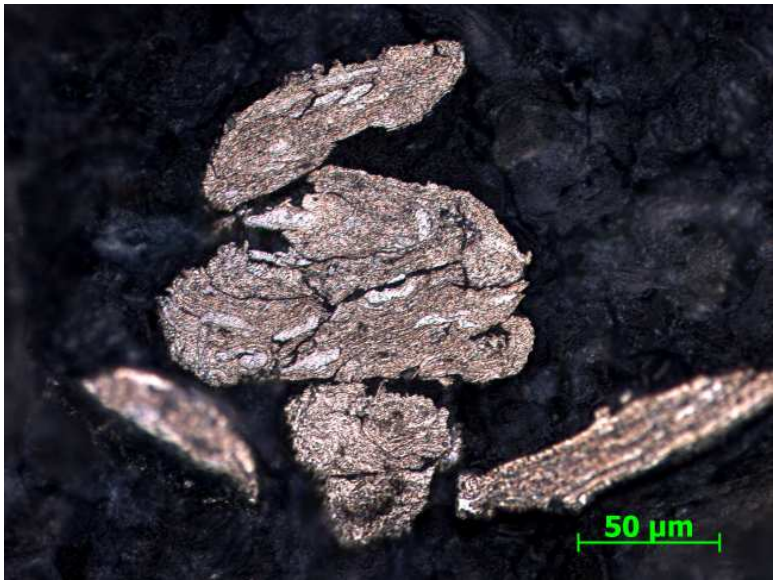

Figure 9. Photomicrograph of Ni with 10v.% Ni-W powder particles that have been attritor milled for 3 hours. The extra milling time allowed for smaller amorphous particles as compared with those in Figure 8. These particles (the lightest areas in the micrograph) have become embedded within Ni particles.

Aspect Ratio of Reinforcement Particles				
Sintering time (hrs.)	1 hour attritor mill		3 hour attritor mill	
	average	std. dev.	average	std. dev.
10	1.79	0.96	2.15	1.09
30	1.64	0.80	2.06	1.10
50	1.61	0.75	1.77	0.89

Table 2. Calculations of reinforcement aspect ratios through SEM image analysis in ImageJ. Particles found to be one square pixel in size were discarded, as the resolution was insufficient to yield any aspect ratio other than 1.

In both sets of samples there is a trend towards decreasing volume fraction of tungsten-rich reinforcement with increasing sintering time. Appendix A shows the results of histogram analysis. In deciding the range of gray values to count, spot histograms were generated for areas of interest in each set of samples. For the one hour attritor-blended samples, the range of gray values counted was 107–255; for the three hour samples, the range was 155–255. While DSC analysis revealed the onset to recrystallization to occur near 728ºC, temperature was being increased at 30 K/min during the test. Time is an important factor in kinetics, however, and the histogram analysis points toward a 600ºC sintering temperature being sufficient to effect recrystallization.

Another noticeable difference between the one- and three-hour attritor blended samples is the distinctness of the microconstituents. Samples milled for one hour result three microconstituents: nickel-rich matrix grains (darkest areas in SEM images), two-phase reinforcement particles (lightest areas in SEM images), and reinforcement particles that have either recrystallized or did not contain sufficient tungsten atoms to amorphize (medium areas). Samples milled for three hours, however, are less distinct. Reinforcement particles are still present, but elsewhere there exists a vague gradient between the nickel-rich matrix grains and the remaining particles. While the extra two

hours of milling allows for more diffusion between matrix and reinforcement particles, and may account for some of the difference, a more likely explanation is that the samples became contaminated during sintering. Particle boundary contamination would prevent diffusion in the one hour sample as the individual constituents remained separated after milling, but three hours of milling allowed for sufficient fracturing and welding that most amorphous Ni-W was contained within nickel powder particles. Thus, diffusion was able to proceed within each powder particle in the samples that were milled for three hours.

Amount of porosity is another factor impacted by attritor milling time. To analyze this, Adobe Photoshop was used to adjust the tonal curve of the image. By shifting the white point input to 80, most gray levels become white and only black areas remain. From this modified image, gray values with a range of 0–100 were counted using the corresponding histogram. The results of this analysis are shown in Appendix A. Porosity shows a slight decrease with increasing sintering time, as expected. However, compared with the porosity of the as-compacted samples, fifty hours of sintering is only marginally more effective than five hours. Thus, the gain in density may be nullified by the decrease in volume fraction of reinforcement particles.

Examination of the SEM images reveals that the tungsten-rich reinforcement particles are actually composites of nanoscale tungsten-rich sub-particles surrounded by a nickel-rich matrix. A back of the envelope calculation using EDS data (see Appendix C) results in a sub-particle composition of approximately 50% W, which is far more than expected in amorphous Ni-W. Thus it is probable that the sub-particles are in fact intermetallic, and the two-phase reinforcement particles are the result of diffusion and crystallization during the sintering stage that exposed the compacted sample to 600ºC temperatures for at least five hours.

The Ni-W phase diagram shows that intermetallic NiW is the equilibrium phase of equimolar Ni-W. Given the complication of tungsten diffusing into the nickel-rich matrix, lower tungsten content would be expected in the reinforcement particles. A

decrease in tungsten moves the particles into a two-phase region of NiW and Ni_4W, which is supported by the SEM images and calculations in Appendix C.

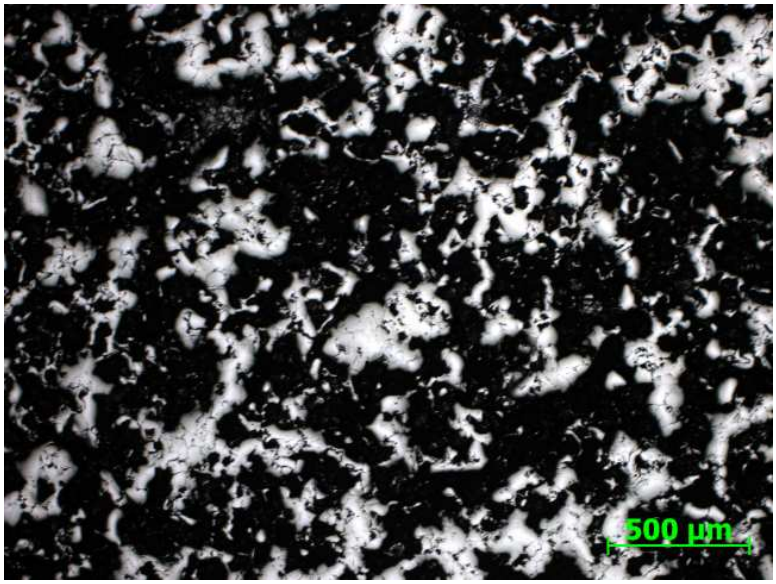

Figure 10. Photomicrograph of as-compacted Ni with 10v.% Ni-W after being attritor milled for 1 hour. Black areas are pores.

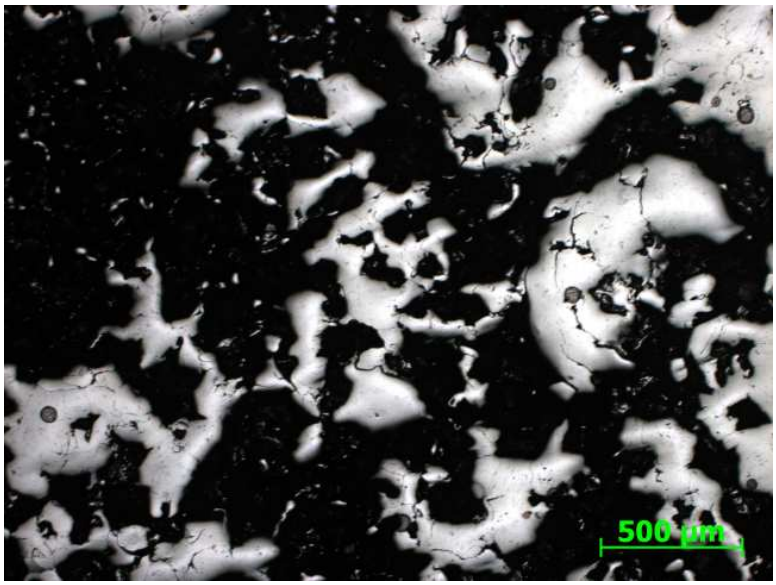

Figure 11. Photomicrograph of as-compacted Ni with 10v.% Ni-W after being attritor milled for 3 hours. Black areas are pores.

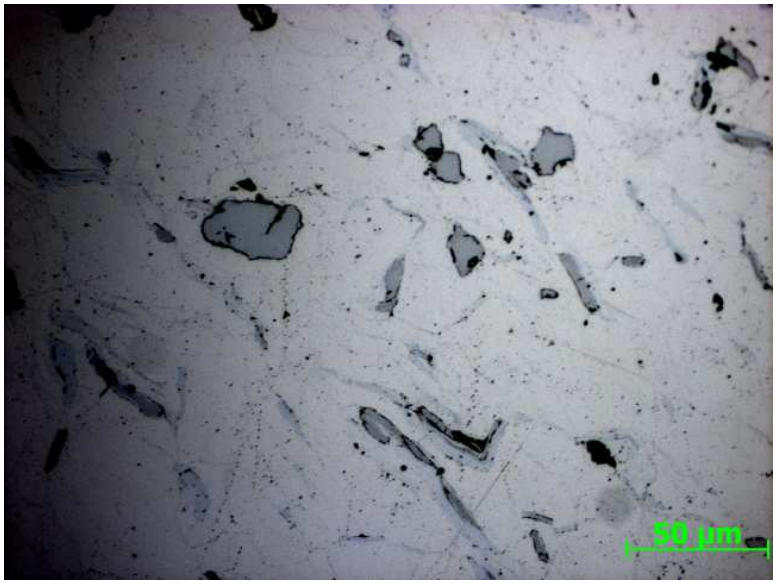

Figure 12. Photomicrograph of a composite of Ni with 10v.% Ni-W after being attritor milled for 1 hour and sintered for 5 hours. Darkest particles are the most tungsten-rich; the matrix is nickel-rich.

Figure 13. Photomicrograph of a composite of Ni with 10v.% Ni-W after being attritor milled for 1 hour, sintered for 5 hours and etched. Lightest particles are most tungsten-rich.

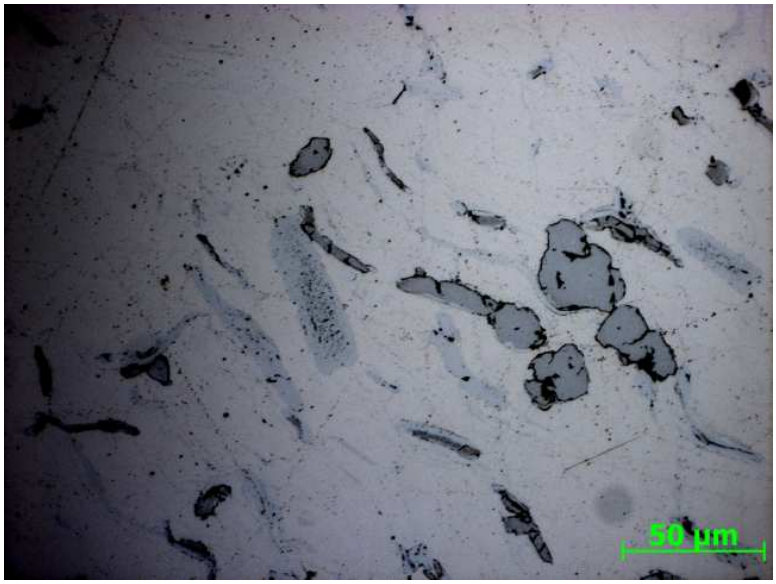

Figure 14. Photomicrograph of a composite of Ni with 10v.% Ni-W after being attritor milled for 1 hour and sintered for 10 hours. Darkest particles are the most tungsten-rich; the matrix is nickel-rich.

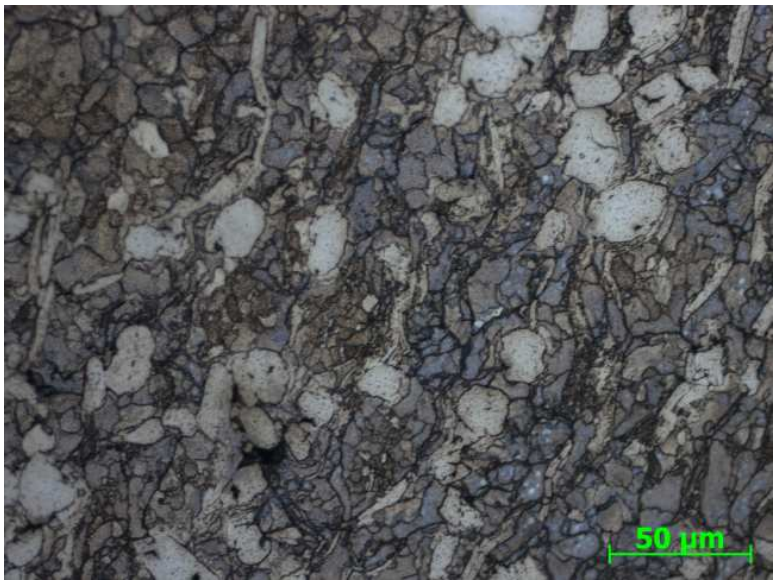

Figure 15. Photomicrograph of a composite of Ni with 10v.% Ni-W after being attritor milled for 1 hour, sintered for 10 hours and etched.

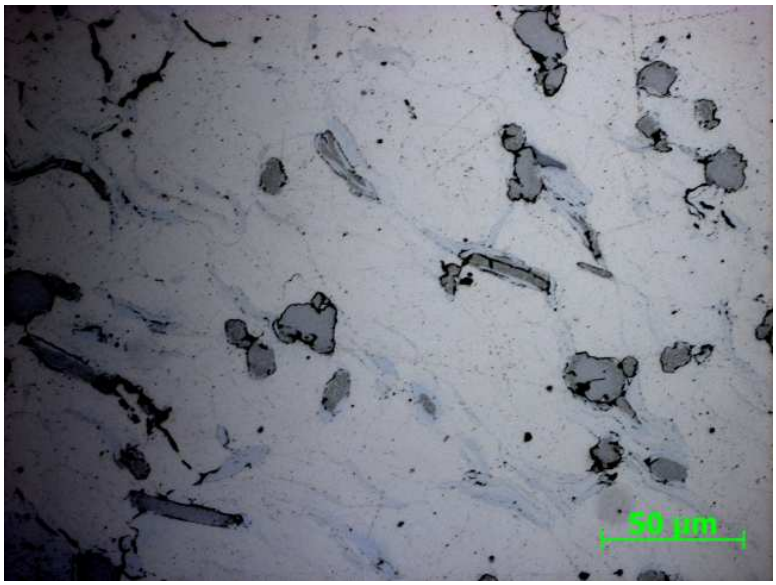

Figure 16. Photomicrograph of a composite of Ni with 10v.% Ni-W after being attritor milled for 1 hour and sintered for 20 hours. Darkest particles are the most tungsten-rich; the matrix is nickel-rich.

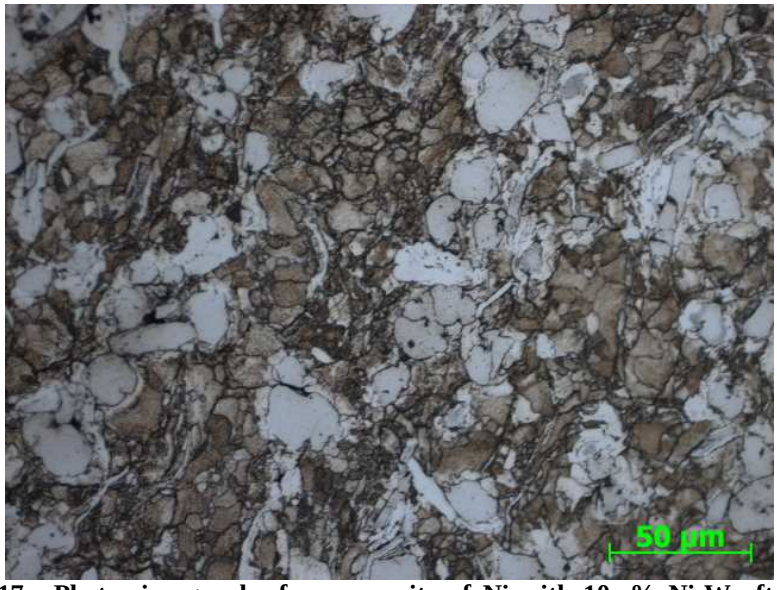

Figure 17. Photomicrograph of a composite of Ni with 10v.% Ni-W after being attritor milled for 1 hour, sintered for 20 hours and etched.

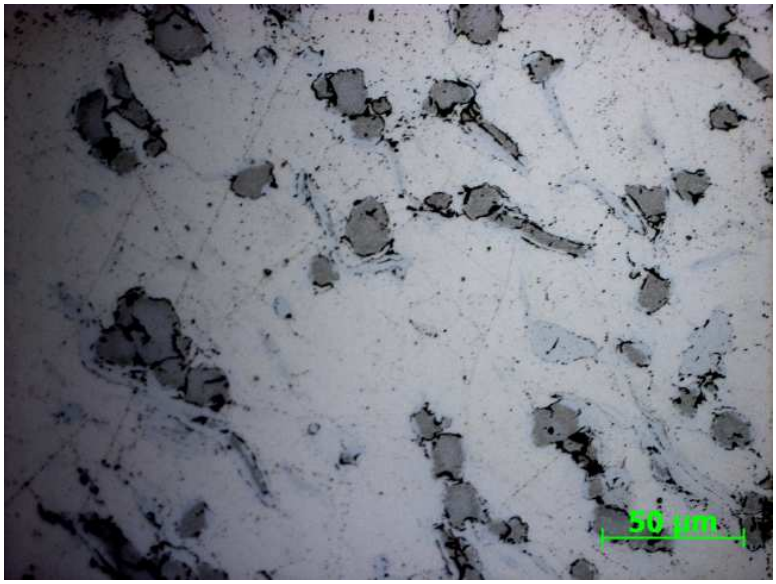

Figure 18. Photomicrograph of a composite of Ni with 10v.% Ni-W after being attritor milled for 1 hour and sintered for 30 hours. Darkest particles are the most tungsten-rich; the matrix is nickel-rich.

Figure 19. Photomicrograph of a composite of Ni with 10v.% Ni-W after being attritor milled for 1 hour, sintered for 30 hours and etched.

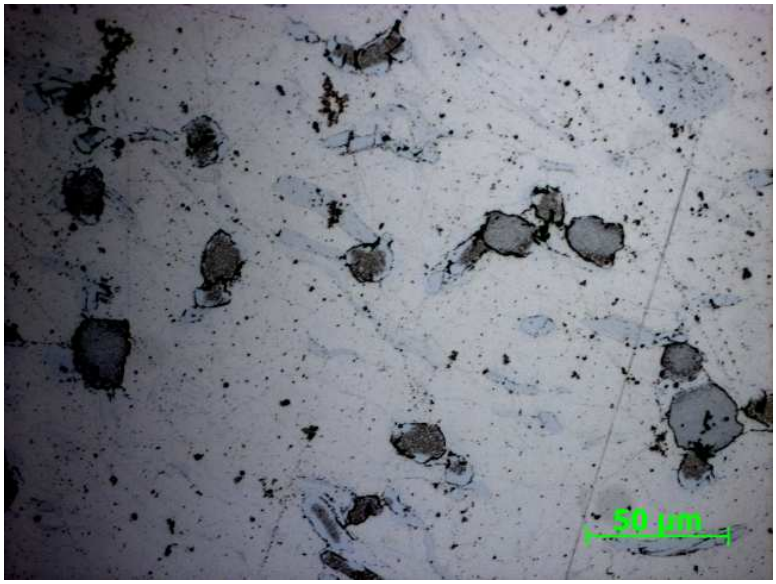

Figure 20. Photomicrograph of a composite of Ni with 10v.% Ni-W after being attritor milled for 1 hour and sintered for 50 hours. Darkest particles are the most tungsten-rich; the matrix is nickel-rich.

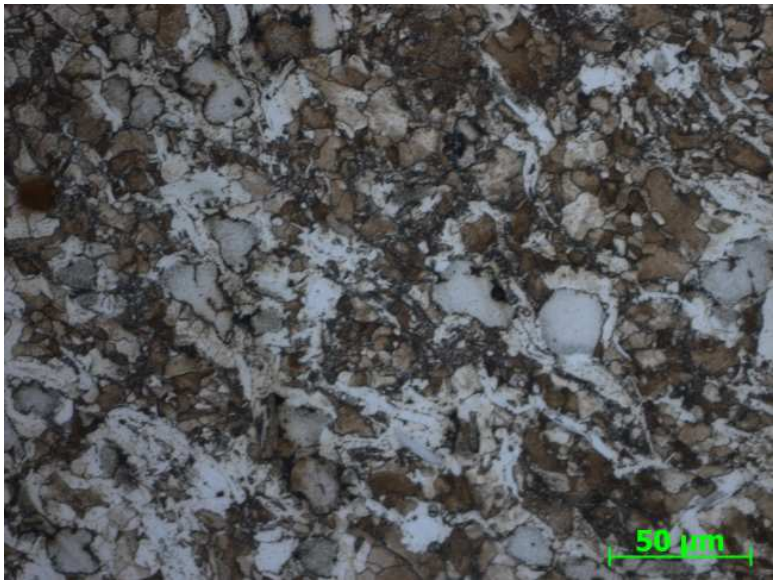

Figure 21. Photomicrograph of a composite of Ni with 10v.% Ni-W after being attritor milled for 1 hour, sintered for 50 hours and etched.

Figure 22. Photomicrograph of a composite of Ni with 10v.% Ni-W after being attritor milled for 3 hours and sintered for 5 hours. Darkest particles are the most tungsten-rich; the matrix is nickel-rich. Tungsten-rich particles are reduced in size and volume percentage as compared with samples attritor milled for 1 hour.

Figure 23. Photomicrograph of a composite of Ni with 10v.% Ni-W after being attritor milled for 3 hours and sintered for 10 hours. Darkest particles are the most tungsten-rich; the matrix is nickel-rich. Tungsten-rich particles are reduced in size and volume percentage as compared with samples attritor milled for 1 hour.

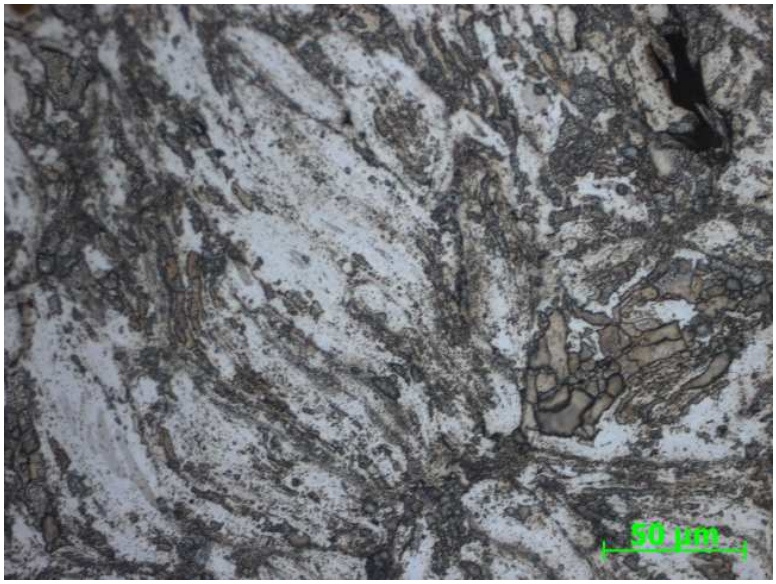

Figure 24. Photomicrograph of a composite of Ni with 10v.% Ni-W after being attritor milled for 3 hours, sintered for 10 hours and etched.

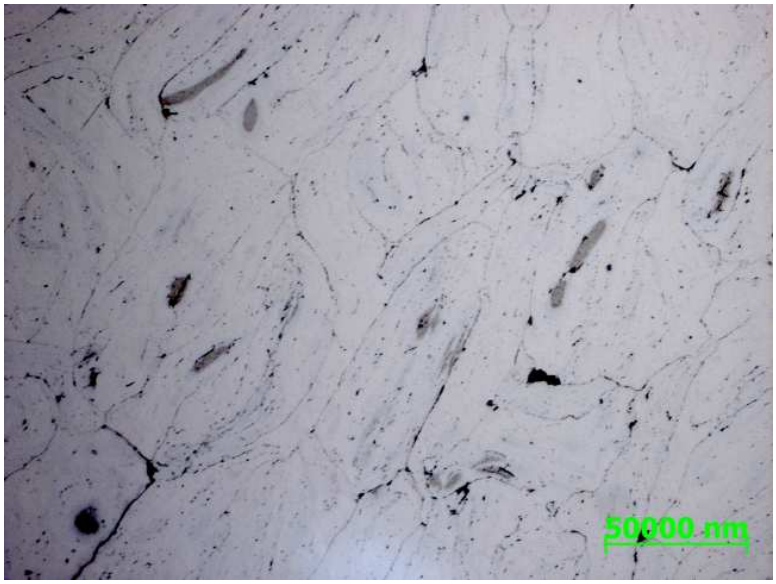

Figure 25. Photomicrograph of a composite of Ni with 10v.% Ni-W after being attritor milled for 3 hours and sintered for 20 hours. Darkest particles are the most tungsten-rich; the matrix is nickel-rich. Tungsten-rich particles are reduced in size and volume percentage as compared with samples attritor milled for 1 hour.

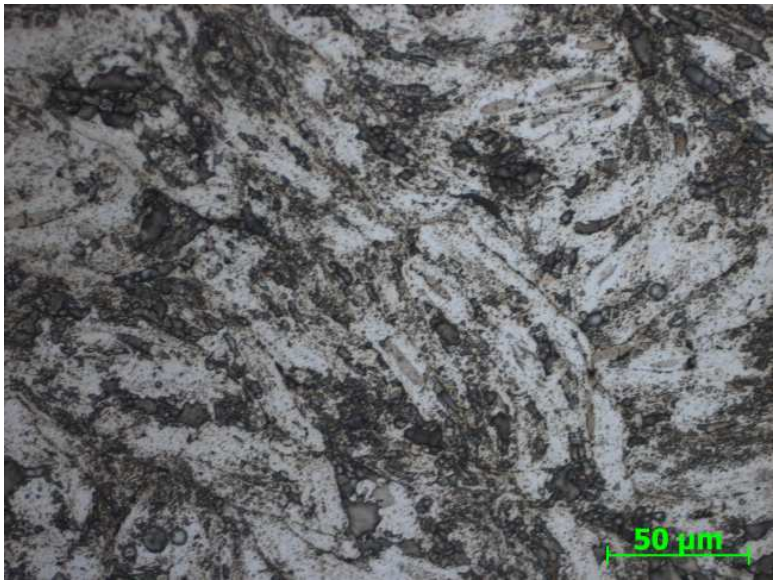

Figure 26. Photomicrograph of a composite of Ni with 10v.% Ni-W after being attritor milled for 3 hours, sintered for 20 hours and etched.

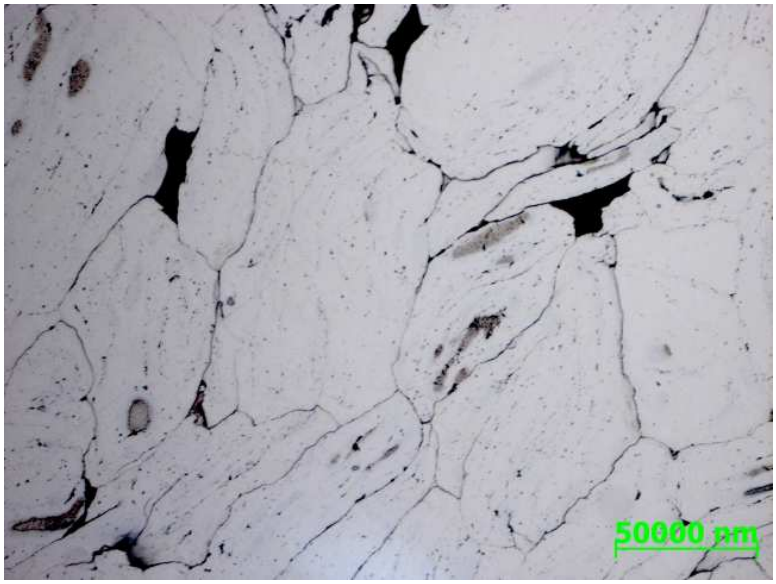

Figure 27. Photomicrograph of a composite of Ni with 10v.% Ni-W after being attritor milled for 3 hours and sintered for 30 hours. Darkest particles are the most tungsten-rich; the matrix is nickel-rich. Tungsten-rich particles are reduced in size and volume percentage as compared with samples attritor milled for 1 hour.

Figure 28. Photomicrograph of a composite of Ni with 10v.% Ni-W after being attritor milled for 3 hours, sintered for 30 hours and etched.

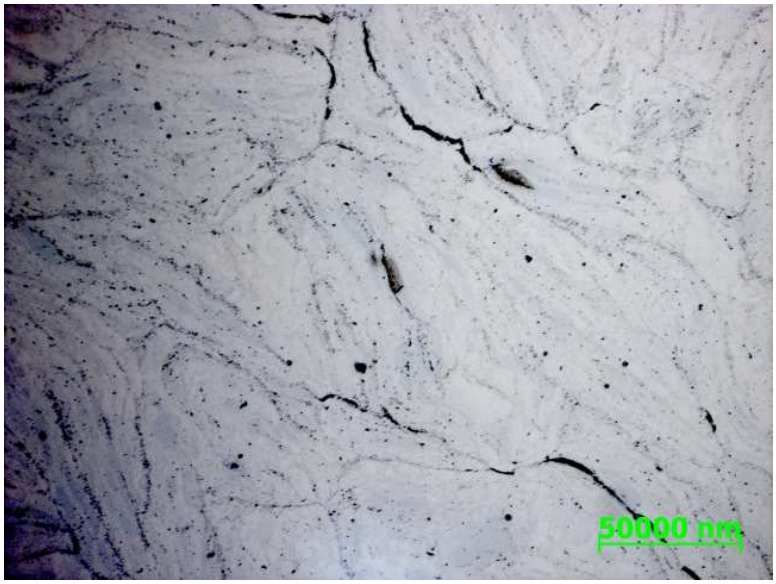

Figure 29. Photomicrograph of a composite of Ni with 10v.% Ni-W after being attritor milled for 3 hours and sintered for 50 hours. Darkest particles are the most tungsten-rich; the matrix is nickel-rich. Tungsten-rich particles are reduced in size and volume percentage as compared with samples attritor milled for 1 hour.

Figure 30. Photomicrograph of a composite of Ni with 10v.% Ni-W after being attritor milled for 3 hours, sintered for 50 hours and etched.

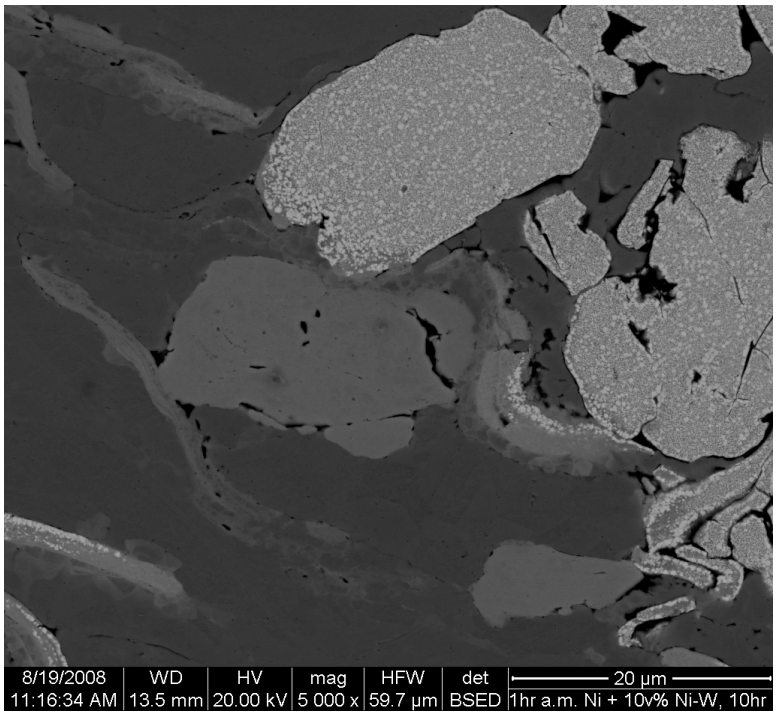

Figure 31. Scanning electron micrograph of a composite of Ni with 10v.% Ni-W after being attritor milled for 1 hour and sintered for 10 hours. Lightest areas are tungsten-rich; darkest areas are nickel-rich.

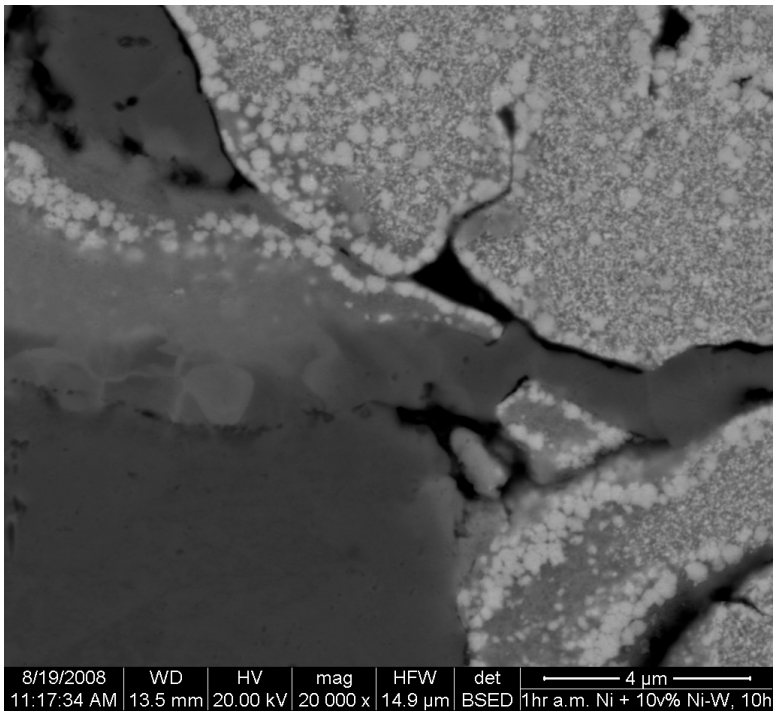

Figure 32. Scanning electron micrograph of a composite of Ni with 10v.% Ni-W after being attritor milled for 1 hour and sintered for 10 hours. The light subparticles are tungsten-rich intermetallics and the result of recrystallization of amorphous Ni-W.

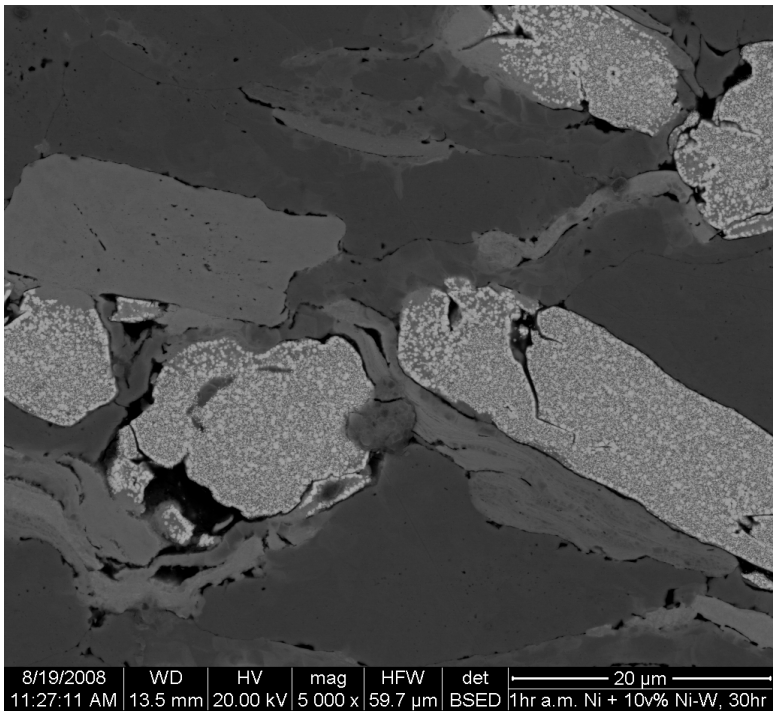

Figure 33. Scanning electron micrograph of a composite of Ni with 10v.% Ni-W after being attritor milled for 1 hour and sintered for 30 hours. Lightest areas are tungsten-rich; darkest areas are nickel-rich.

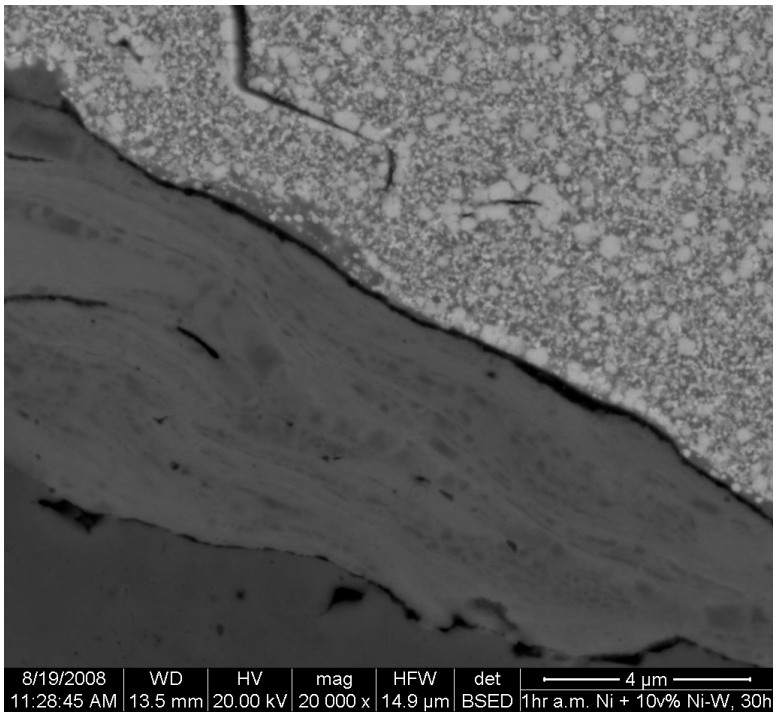

Figure 34. Scanning electron micrograph of a composite of Ni with 10v.% Ni-W after being attritor milled for 1 hour and sintered for 30 hours. The light subparticles are tungsten-rich intermetallics and the result of recrystallization of amorphous Ni-W.

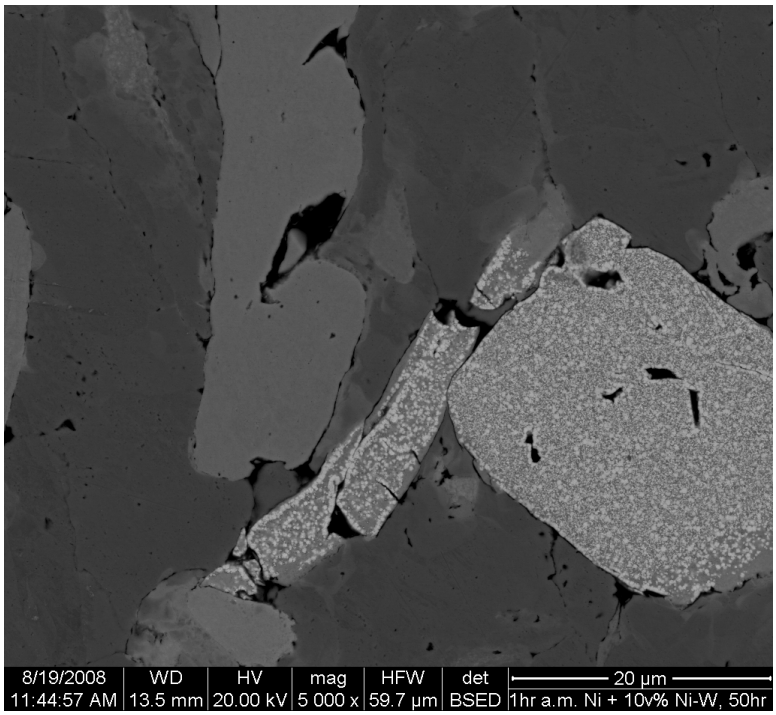

Figure 35. Scanning electron micrograph of a composite of Ni with 10v.% Ni-W after being attritor milled for 1 hour and sintered for 50 hours. Lightest areas are tungsten-rich; darkest areas are nickel-rich.

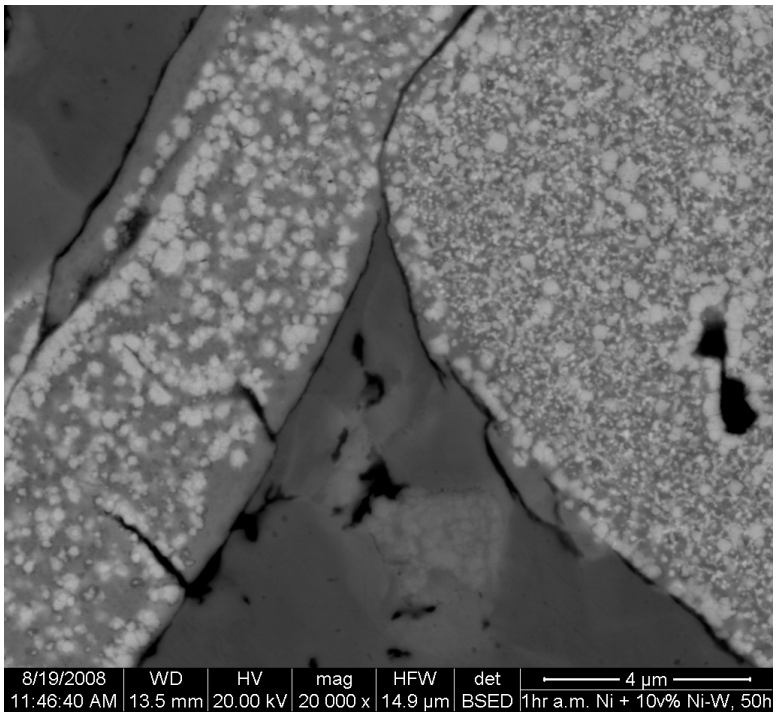

Figure 36. Scanning electron micrograph of a composite of Ni with 10v.% Ni-W after being attritor milled for 1 hour and sintered for 50 hours. The light subparticles are tungsten-rich intermetallics and the result of recrystallization of amorphous Ni-W.

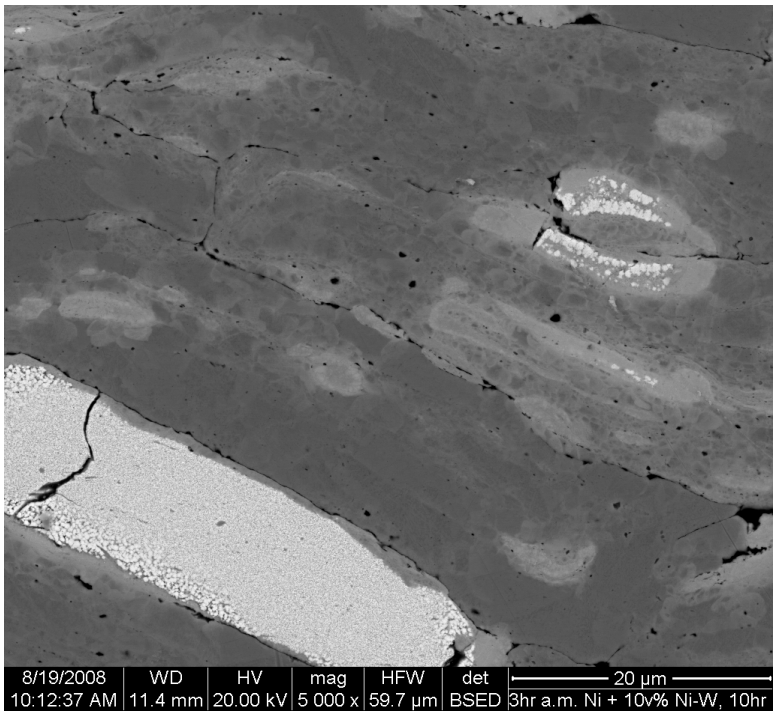

Figure 37. Scanning electron micrograph of a composite of Ni with 10v.% Ni-W after being attritor milled for 3 hours and sintered for 10 hours. Lightest areas are tungsten-rich; darkest areas are nickel-rich.

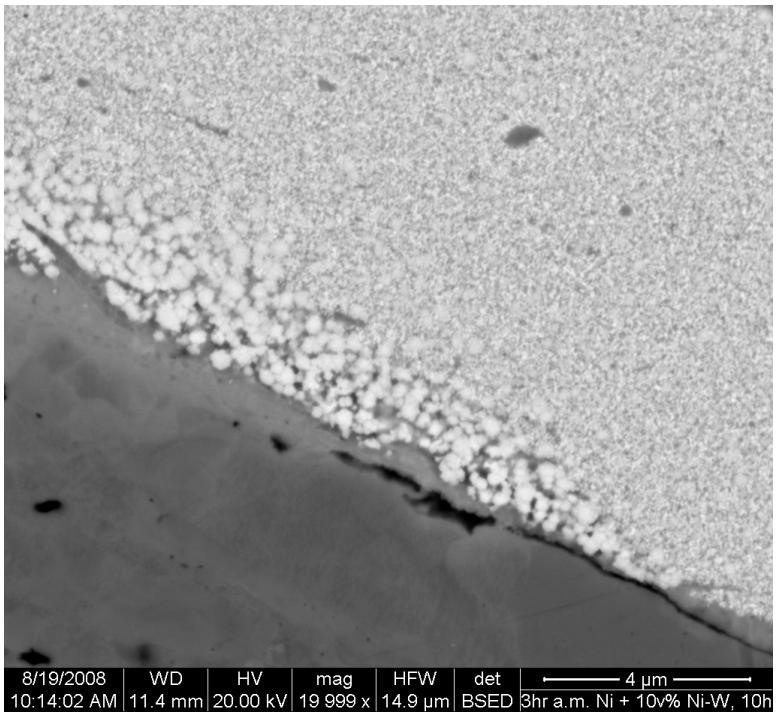

Figure 38. Scanning electron micrograph of a composite of Ni with 10v.% Ni-W after being attritor milled for 3 hours and sintered for 10 hours. The light subparticles are tungsten-rich intermetallics and the result of recrystallization of amorphous Ni-W.

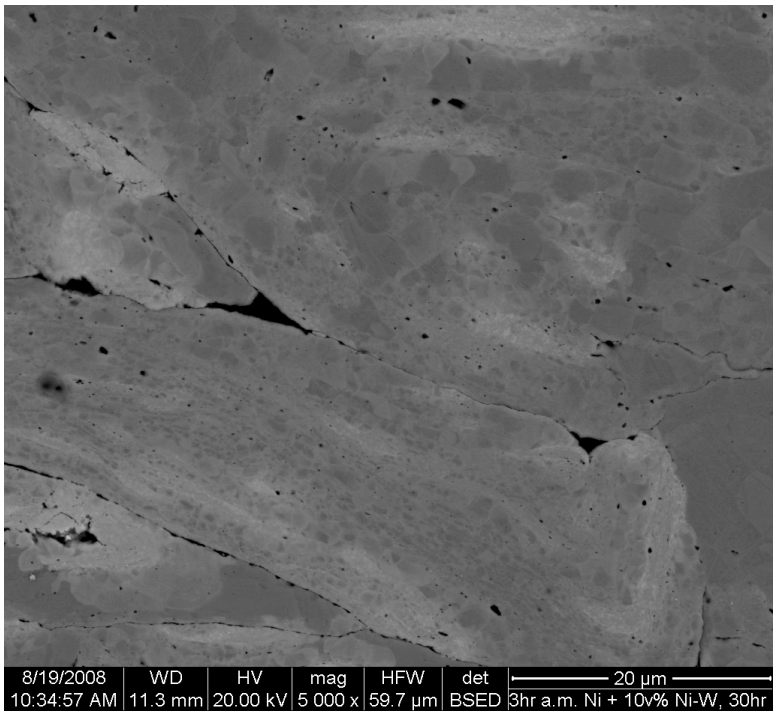

Figure 39. Scanning electron micrograph of a composite of Ni with 10v.% Ni-W after being attritor milled for 3 hours and sintered for 30 hours. Lightest areas are tungsten-rich; darkest areas are nickel-rich.

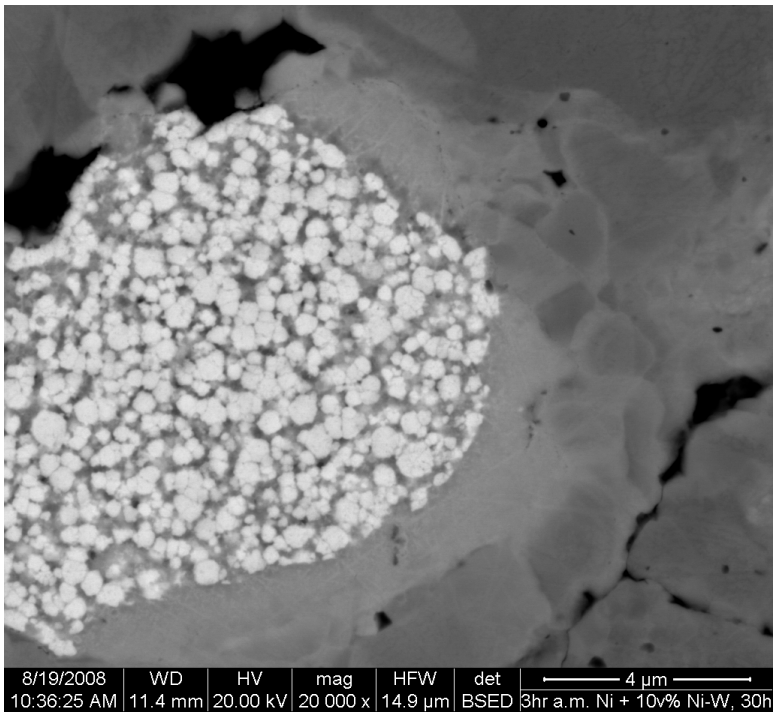

Figure 40. Scanning electron micrograph of a composite of Ni with 10v.% Ni-W after being attritor milled for 3 hours and sintered for 30 hours. The light subparticles are tungsten-rich intermetallics and the result of recrystallization of amorphous Ni-W.

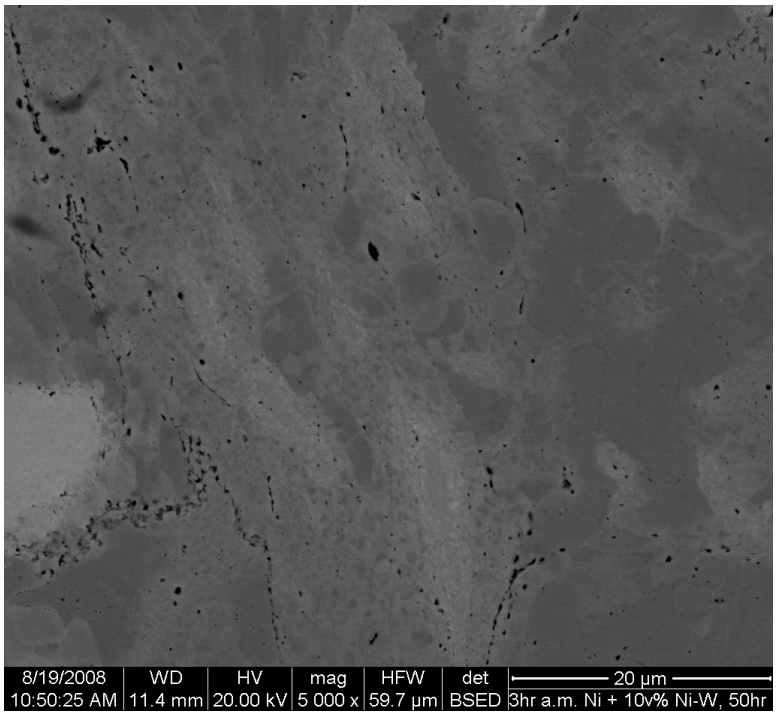

Figure 41. Scanning electron micrograph of a composite of Ni with 10v.% Ni-W after being attritor milled for 3 hours and sintered for 50 hours. Lightest areas are tungsten-rich; darkest areas are nickel-rich.

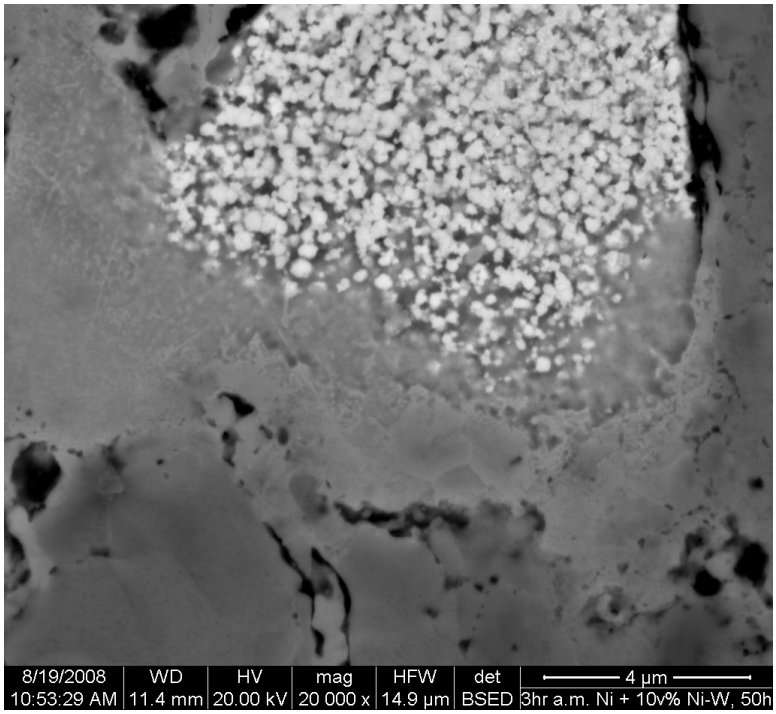

Figure 42. Scanning electron micrograph of a composite of Ni with 10v.% Ni-W after being attritor milled for 3 hours and sintered for 50 hours. The light subparticles are tungsten-rich intermetallics and the result of recrystallization of amorphous Ni-W.

4.2.4 Vickers Hardness

Vickers macrohardness testing resulted in values (see Appendix B) that were lower across the board than the value for pure nickel of approximately 130, previously reported in similar work by Wensley [25]. Wensley's samples were hot-isostatic pressed, however, and this difference in compaction methods may account for the difference in values. Figure 44 shows a representative micrograph of the pyramidal indentations. Instead of clean edge lines along the rim of the indentation, grains that were partially indented seem to have separated from surrounding grains and sunk into the depression. This is likely a result of contamination, presumed to have occurred during sintering, which prevented good bonding between powder particles.

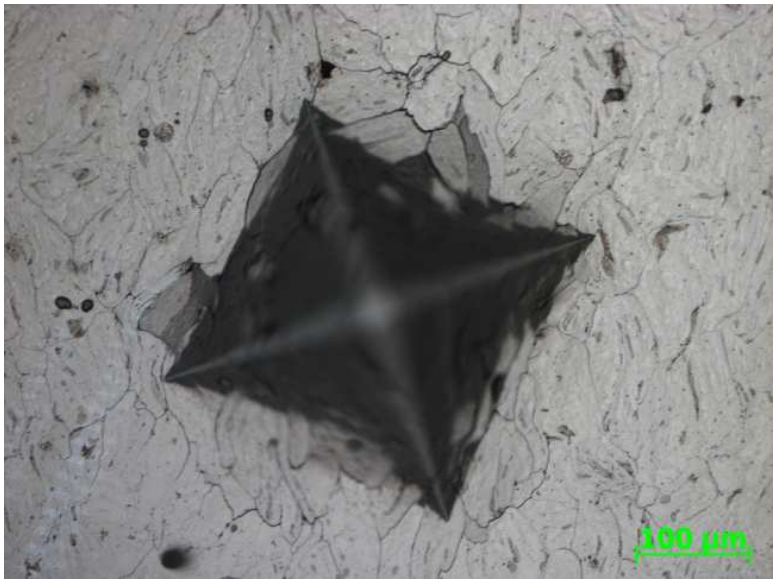

Figure 43. Photomicrograph of a composite of Ni with 10v.% Ni-W after being attritor milled for 3 hours and sintered for 5 hours. Vickers macrohardness testing shows partially indented particles separating from adjacent paricles.

5. Strengthening Model

Though hardness data was compromised by the presence of contamination between powder particles, a model to predict strengthening can be developed by inserting calculated parameter values in strengthening equations for the various relevant mechanisms.

5.1 Boundary Strengthening

A well known strengthening mechanism called boundary strengthening involves the impedance of dislocation motion at grain boundaries. As grains rarely meet coherently, dislocations will require extra energy to overcome the stress field at a grain boundary and change slip direction in the adjacent grain. When the energy is not sufficient, dislocations pile up at the grain boundaries and the material is strengthened. A similar mechanism will be present in particle-reinforced composites, where dislocations cannot easily move through the second phase particles [68]. Like the Hall-Petch equation that predicts grain boundary strengthening, boundary strengthening is related to the square root of the inverse interparticle spacing. Four equations have been devised to predict boundary strengthening, each pertaining to separate mechanical behavior. Since the mechanical testing in this work was not sufficient to determine the material's behavior, the equation chosen by Wensley for his work on the same material will be used here. The boundary strengthening contribution is

$$\Delta\sigma = \alpha'' \sqrt{\frac{G_m^{\,2} \cdot b}{5L_{e-e}}} \qquad (2)$$

where α" is a fitting parameter approximately equal to 1, G_m is the shear modulus of the matrix, b is the magnitude of the Burgers vector and L_{e-e} is the reinforcement interparticle spacing [68].

The reinforcement interparticle spacing was found through image analysis using ImageJ and a procedure developed by Alex Wensley (see [25]). Results are shown in Table 3; the values are much larger than those calculated for other strengthening mechanisms. The low value for the sample attritor milled for three hours and sintered for fifty hours is the result of massive dissolution of tungsten into the matrix, showing that boundary strengthening is much more effective than solid solution strengthening in this system.

Boundary Strengthening (MPa)			
	sintering time (hours)		
	10	30	50
1 hr attritor mill	66.845	62.535	55.664
3 hr attritor mill	73.483	79.873	33.872

Table 3. The expected increase in tensile strength due to boundary strengthening was calculated for each attritor milling time/sintering time combination. Boundary strengthening is expected to be the dominant strengthening mechanism in this materials system.

5.2 Orowan Strengthening

Where reinforcement particles are sufficiently small to exist entirely within grains of the matrix material, a dislocation that encounters such a particle may realize an energy savings by bowing around the particle and reconnecting on the other side, as opposed to moving through the particle. This bowing and reconnecting will leave a dislocation loop

surrounding the reinforcement particle, and the additional stress fields increase the likelihood that subsequent dislocations will be arrested near the interface [22, 69].

The Orowan equation predicts a composite strength that is related to the inverse of the interparticle spacing,

$$\sigma_c \cong \sigma_m + \frac{3G_m b}{L_{e-e}} \tag{3}$$

where σ_c is the yield stress of the composite and σ_m is the yield stress of the matrix. The equation falls short, predicting an inordinately high yield stress, as the reinforcement interparticle spacing approaches zero. This has been rectified by the Ashby-Orowan equation, which takes into account that a sufficiently small reinforcement particle is essentially a solute atom and does not lead to the formation of Orowan loops. The equation is

$$\Delta\sigma = \frac{2.4G_m b}{2\pi(1-\upsilon)^{0.5}} \cdot \frac{\ln(d_r / r_0)}{L_{e-e}} \tag{4}$$

where υ is the Poisson's ratio of the matrix, d_r is the reinforcement diameter and r_0 is the dislocation core radius. Table 4 shows the results.

Orowan Strengthening (MPa)			
	sintering time (hours)		
	10	30	50
1 hr attritor mill	3.027	2.672	2.113
3 hr attritor mill	3.560	4.212	0.757

Table 4. The expected increase in tensile strength due to Orowan strengthening was calculated for each attritor milling time/sintering time combination. Values constitute a much less significant increase in strength with respect to boundary strengthening.

5.3 Solid Solution Strengthening

Stress fields created by the presence of solute atoms can interact with those associated with dislocations, causing impedance of dislocation motion [68]. Since dissolution of tungsten from the reinforcement particles occurred during sintering, it is necessary to consider the strengthening contribution of tungsten solute atoms in the nickel matrix. The equation governing this strengthening mechanism is

$$\Delta\tau_y = G_m b \varepsilon^{3/2} c^{1/2} \tag{5}$$

where $\Delta\tau_y$ is the change in shear yield strength, c is the concentration of solute atoms and $\varepsilon = \left|\left(r_{matrix} - r_{solute}\right)/r_{matrix}\right|$ is the misfit strain [70].

To determine the strengthening due to solute atoms, ImageJ was used to produce a histogram for each SEM image, and the corresponding data (i.e. pixel count at each gray value) was exported to Microsoft Excel. Compositions from local EDS analysis were assigned to their corresponding gray values and remaining values were fit linearly. Strengthening was then calculated for each gray value and rule of mixtures applied to determine the overall strengthening contribution in each sample due to solid solution strengthening. (Pores and reinforcement particles were digitally removed from the image so that only the matrix was considered.) Results are shown in Table 5.

5.4 The Effect of Aspect Ratio on Strengthening

Where improved strength is desired, high aspect ratio reinforcement particles can be effective provided they are aligned in the loading direction. Whether the fibers are continuous or discontinuous, such particles' main strengthening mechanism is not related to microscopic interactions with the matrix, but rather load transfer. Here the matrix exists to transfer the load to the reinforcement and hold the fibers together [68].

Solid Solution Strengthening (MPa)			
	sintering time (hours)		
	10	30	50
1 hr attritor mill	0.306	0.404	0.566
3 hr attritor mill	0.697	0.811	0.574

Table 5. The expected increase in shear strength due to solid solution strengthening was calculated for each attritor milling time/sintering time combination. Values across the board are less than 1 MPa; thus, it is apparent that dissolution of the tungsten during sintering has a deleterious effect on the mechanical properties of the composite under study, given that reinforcement particles are consumed in the process.

Equations have been developed to predict the strength of composites reinforced with both continuous and discontinuous fibers. However, these equations are not able to separate the contributions of various strengthening mechanisms. Though load transfer is the main strengthening mechanism in such composites, other mechanisms also contribute to strengthening. Boundary strengthening, for example, can be important, as the high surface-area-to-volume ratio of a fiber-reinforced composite implies a low interparticle spacing as compared to a composite reinforced with equiaxed particles (where the volume fraction of the reinforcement is equivalent).

Though no equations have been developed to predict strengthening solely due to load transfer, some statements about its relative effectiveness in this system can be made. The ability of a discontinuous fiber to carry a load relative to a continuous fiber is dependent on its length, as load-carrying ability is decreased near the fiber ends. An equation for a critical aspect ratio has been put forth, but is dependent on applied stress and therefore not estimated here [68]. Typical critical aspect ratio values, however, are many times greater than the values seen in this work. Also detracting from load transfer is the misalignment of the reinforcement particles. Alignment was not controlled in this

study, and the particles are assumed to be randomly oriented. There is a critical angle (typically $\leq 10^{o}$) beyond which strength decreases rapidly as matrix shear becomes a more favorable failure mode than reinforcement fracture [68]. These factors make it significantly less likely that load transfer will be a strengthening mechanism of consequence in this work.

5.5 Comment on Results

Plots showing the three calculated strengthening contributions in each attritor-milled sample are provided in Figures 45 and 46. The two samples are compared in Figure 47. The contributions from Orowan strengthening and solid solution strengthening are small due to large particle size and similar atomic radii, respectively. Boundary strengthening is the prevailing mechanism, though the contribution generally decreases with increased sintering time as particles are lost due to diffusion of the tungsten into the matrix.

Experimental values in Wensley's study were shown to be approximately double the calculated values, and increased with reinforcement volume percent despite the accompanying increase in porosity [25]. Other, uncalculated strengthening mechanisms likely account for the difference. In these composites, additional strengthening could be imparted through coefficient of thermal expansion differences, grain boundary refinement and shear load transfer. The conservativeness of the boundary strengthening equation may also play a role (i.e. other models exist that predict greater strengthening, but they cannot be employed without certainty of the composite's failure mechanism).

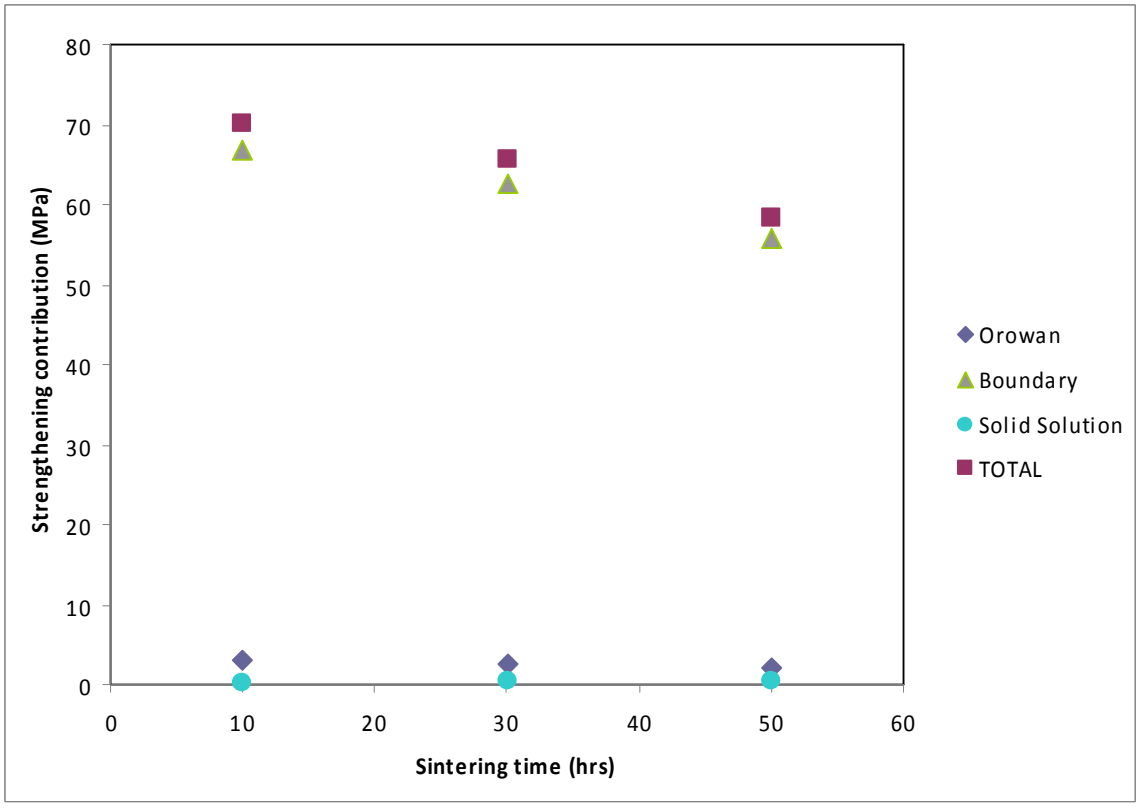

Figure 44. Plot of predicted strengthening contributions in the samples attritor-milled for one hour. Boundary strengthening is the dominant mechanism, as the particles are too large for substantial Orowan strengthening and the atomic radii too similar for substantial solid solution strengthening.

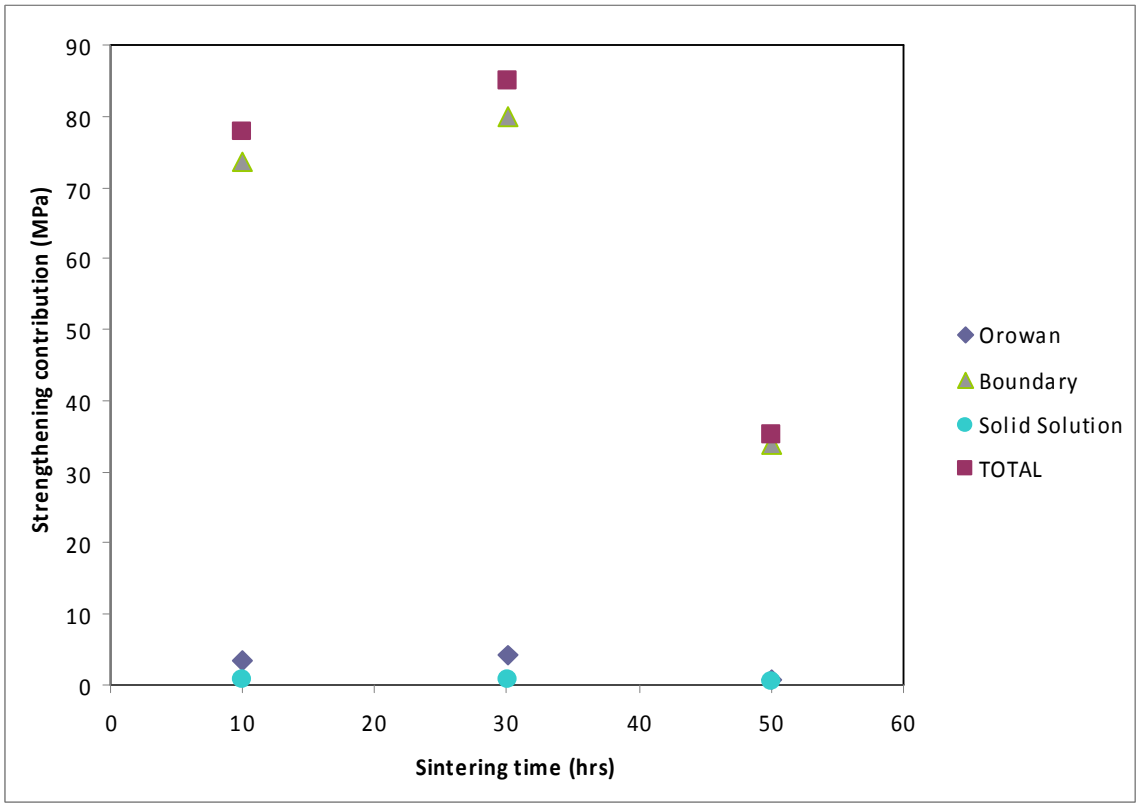

Figure 45. Plot of predicted strengthening contributions in the samples attritor-milled for three hour. Boundary strengthening is the dominant mechanism, as the particles are too large for substantial Orowan strengthening and the atomic radii too similar for substantial solid solution strengthening.

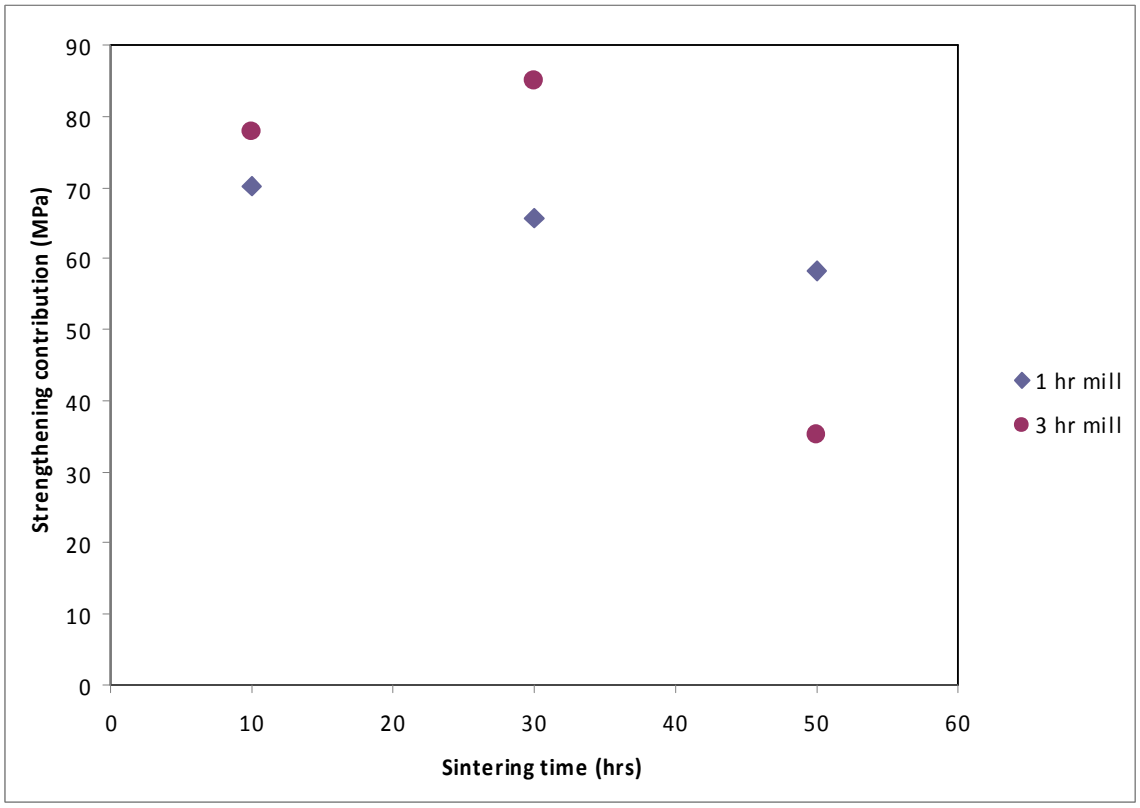

Figure 46. Plot of predicted strengthening contributions in the two attritor-milled samples. Greater strengthening is predicted in the three-hour attritor-milled sample for lower sintering times (due to decreased interparticle spacing), but not after fifty hours of sintering (due to massive diffusion of tungsten into the matrix).

6. Summary

Equimolar amorphous Ni-W powder particles containing crystallites of W were produced using the mechanical alloying process. The mechanically alloyed powder was subsequently attritor-milled with pure nickel powder for either one or three hours, compacted by combustion-driven compaction and sintered at 600ºC for up to fifty hours. Prolonged sintering led to crystallization of the amorphous reinforcement particles. Also apparent, through EDS mapping, was greater dissolution of tungsten in samples blended for three hours compared with those blended for one hour. Vickers macrohardness tests on the sintered composites yielded lower-than-expected values due to poor bonding between the particles, which is believed to be the result of contamination introduced during sintering.

Modeling of the strengthening contributions predicts that boundary strengthening is the dominant mechanism in these composites, while Orowan strengthening and solid solution strengthening contribute minimally. Though the contribution from shear load transfer cannot be modeled independently, the samples reinforced with particles of higher aspect ratio should result in increased strengthening due in part to decreased interparticle spacing. Ultimately, however, the increases achieved in the reinforcement aspect ratio, coupled with the particles' random orientation, are likely insufficient to cause significant strengthening by shear load transfer.

7. References

1. Kampe, S.L., *Class lecture*, in *MSE5104 - Composite Materials*. 2007, Virginia Polytechnic Institute & State University, Blacksburg, VA.
2. Klement, W., R.H. Willens, and P.O.L. Duwez, *Non-crystalline Structure in Solidified Gold-Silicon Alloys.* Nature, 1960. **187**(4740): p. 869-870.
3. Cheng, Y.T., W.L. Johnson, and M.A. Nicolet. *Studies on the rules for amorphous phase formation by ion-mixing in metallic systems*. 1985. Los Angeles, CA, USA.
4. Brimhall, J.L., H.E. Kissinger, and L.A. Charlot, *Amorphous phase formation in irradiated intermetallic compounds.* Radiation Effects, 1983. **77**(3-4): p. 273-93.
5. Schwarz, R.B. and W.L. Johnson, *Formation of an amorphous alloy by solid-state reaction of the pure polycrystalline metals.* Physical Review Letters, 1983. **51**(5): p. 415-18.
6. Benjamin, J.S. and T.E. Volin, *Mechanism of mechanical alloying.* Metallurgical Transactions, 1974. **5**(8): p. 1929-1934.
7. Benjamin, J.S., *Mechanical alloying.* Scientific American, 1976. **234**(5): p. 108-16.
8. Aning, A.O., Z. Wang, and T.H. Courtney, *Tungsten solution kinetics and amorphization of nickel in mechanically alloyed Ni-W alloys.* Acta Metallurgica et Materialia, 1993. **41**(1): p. 165-174.
9. Lee, P.-Y., et al., *Consolidation of amorphous Ni-Zr-Ti-Si powders by vacuum hot-pressing method.* Intermetallics, 2002. **10**(11-12): p. 1277-1282.
10. Mi, S. and T.H. Courtney, *Processing, structure and properties of Ni-W alloys fabricated by mechanical alloying and hot-isostatic pressing.* Scripta Materialia, 1998. **38**(4): p. 637-44.
11. Kawamura, Y., H. Mano, and A. Inoue. *Nanocrystalline aluminum bulk alloys with a high strength of 1420 MPa produced by the consolidation of amorphous powders*. 2001. Sendai, Japan: Elsevier for Board of Directors of Acta Metall.
12. Kim, H.J., et al., *Cu-based bulk amorphous alloys prepared by consolidation of amorphous powders in the supercooled liquid region.* Intermetallics, 2004. **12**(10-11): p. 1109-13.
13. Lee, M.H., et al., *Synthesis of Ni-based bulk amorphous alloys by warm extrusion of amorphous powders.* Journal of Non-Crystalline Solids, 2003. **315**(1-2): p. 89-96.
14. Huang, X. and T. Mashimo, *Metastable BCC and FCC alloy bulk bodies in Fe-Cu system prepared by mechanical alloying and shock compression.* Journal of Alloys and Compounds, 1999. **288**(1-2): p. 299-305.
15. Huang, X.S. and T. Mashimo. *Preparation of Fe-W system metastable alloy bulk body by mechanical alloying and shock compression*. 1999. Kumamoto, Japan: Elsevier.

16. Huang, X. and T. Mashimo, *Metastable alloy bulk bodies in the Fe-W system prepared by mechanical alloying and shock compression.* Journal of Alloys and Compounds, 2000. **296**(1-2): p. 183-90.
17. Mashimo, T., S. Ozaki, and K. Nagayama, *Keyed-powder gun for the oblique-impact shock study of solids in several 10 s of GPa region.* Review of Scientific Instruments, 1984. **55**(2): p. 226-30.
18. Ye, L.L., et al., *Consolidation of MA amorphous NiTi powders by spark plasma sintering.* Materials Science & Engineering A (Structural Materials: Properties, Microstructure and Processing), 1998. **A241**(1-2): p. 290-3.
19. De la Torre, S.D., et al., *Nickel-molybdenum catalysts fabricated by mechanical alloying and spark plasma sintering.* Materials Science & Engineering A (Structural Materials: Properties, Microstructure and Processing), 2000. **A276**(1-2): p. 226-35.
20. Chawla, K.K., *Composite materials : science and engineering*. 1987, New York: Springer-Verlag.
21. Millis, K.D., *Invention of ductile iron...in Millis' own words.* Modern Casting, 1998. **88**(10): p. 41.
22. Clyne, T.W. and P.J. Withers, *An introduction to metal matrix composites*. Cambridge solid state science series. 1993, Cambridge [England]: Cambridge University Press.
23. Martin, J.W., *Micromechanisms in particle-hardened alloys*. 1980: Cambridge. viii+201.
24. Stawovy, M.T. and A.O. Aning, *Processing of amorphous Fe-W reinforced Fe matrix composites.* Materials Science and Engineering A, 1998. **256**(1-2): p. 138-143.
25. Wensley, C.A., *Processing and Properties of Amorphous NiW Reinforced Crystalline Ni Matrix Composites*, in *Materials Science & Engineering*. 2005, Virginia Polytechnic Institute & State University: Blacksburg, VA. p. 50.
26. Suryanarayana, C., *Mechanical alloying and milling.* Progress in Materials Science, 2001. **46**(1-2): p. 1-184.
27. Froes, F.H., et al. *Synthesis of titanium aluminide intermetallics by mechanical alloying*. 1993. San Diego, CA, USA: Publ by Metal Powder Industries Federation, Princeton, NJ, USA.
28. Beaulieu, L., et al., *Nanocomposites in the Sn-Mn-C system produced by mechanical alloying.* Journal of Alloys and Compounds, 2000. **297**(1-2): p. 122-128.
29. Kim, Y.S., et al. *Effect of ceramic dispersions on the high temperature strength of mechanical alloyed MoSi2*. 1991. Boston, MA, USA: Mater. Res. Soc.
30. Kimura, H., K. Hanada, and K. Ishigane. *Mechanical alloying and powder consolidation in SiC and hydroxyapatite*. 2005. Kyoto, Japan: Trans Tech Publications Ltd, Stafa-Zuerich, CH-8712, Switzerland.
31. Farrell, M.P., R.G. Kander, and A.O. Aning, *Polymer blends formed by solid-state mechanical alloying.* Journal of Materials Synthesis and Processing, 1996. **4**(3): p. 151-61.

32. Schultz, J.P., et al. *Processing-structure-property relations of polymer-polymer composites formed by cryogenic mechanical alloying for selective laser sintering applications*. 2000. San Francisco, CA: Materials Research Society.
33. Namboodri, S.L., et al., *Formation of polymer/ceramic composite grain boundary capacitors by mechanical alloying.* Polymer, 1994. **35**(19): p. 4088-4091.
34. Menéndez, E., et al., *Cold compaction of metal-ceramic (ferromagnetic-antiferromagnetic) composites using high pressure torsion.* Journal of Alloys and Compounds, 2007. **434-435**: p. 505-508.
35. Anantharaman, T.R. and C. Suryanarayana, *Review: A decade of quenching from the melt.* Journal of Materials Science, 1971. **6**(8): p. 1111-35.
36. Suryanarayana, C., *Non-equilibrium processing of materials*. Pergamon materials series, v. 2. 1999, Amsterdam; New York: Pergamon.
37. Sundaresan, R. and F.H. Froes, *Mechanical alloying.* Journal of Metals, 1987. **39**(8): p. 22-7.
38. Lee, P.Y., J.L. Yang, and H.M. Lin, *Amorphization behaviour in mechanically alloyed Ni-Ta powders.* Journal of Materials Science, 1998. **33**(1): p. 235-239.
39. Aikin, B.J.M. and T.H. Courtney, *The kinetics of composite particle formation during mechanical alloying.* Metallurgical Transactions A (Physical Metallurgy and Materials Science), 1993. **24A**(3): p. 647-57.
40. *Metallic glasses : papers presented at a seminar of the Materials Science Division of the American Society for Metals, September 18 and 19, 1976*. Metals Park, Ohio: American Society for Metals.
41. Chaudhari, P. and D. Turnbull, *Structure and properties of metallic glasses.* Science, 1978. **199**(4324): p. 11-21.
42. Elliott, R.O. and B.C. Giessen, *On the formation of metallic glasses based on U, Np or Pu.* Acta Metallurgica, 1982. **30**(4): p. 785-789.
43. Liu, B.X., W.S. Lai, and Q. Zhang, *Irradiation induced amorphization in metallic multilayers and calculation of glass-forming ability from atomistic potential in the binary metal systems.* Materials Science & Engineering R: Reports, 2000. **R29**(1-2): p. 1-48.
44. Oesterreicher, H., J. Clinton, and H. Bittner, *Hydrides of La-Ni compounds.* Materials Research Bulletin, 1976. **11**(10): p. 1241-7.
45. Aoki, K., T. Yamamoto, and T. Masumoto, *Hydrogen induced amorphization in RNi2 Laves phases.* Scripta Metallurgica, 1987. **21**(1): p. 27-31.
46. Benedictus, R., et al., *Solid state amorphization in Ni-Ti systems: the effect of structure on the kinetics of interface and grain-boundary amorphization.* Acta Materialia, 1998. **46**(15): p. 5491-5508.
47. Murty, B.S., S. Ranganathan, and M. Mohan Rao, *Solid state amorphization in binary Ti---Ni, Ti---Cu and ternary Ti---Ni---Cu system by mechanical alloying.* Materials Science and Engineering: A, 1992. **149**(2): p. 231-240.
48. Benedictus, R., et al., *Solid state amorphization in the Co-Ti system.* Thin Solid Films, 1999. **345**(2): p. 319-329.
49. Thompson, J.R., C. Politis, and Y.C. Kim, *Properties of materials with a fine length scale: Mechanically alloyed metals and the high temperature superconductor Y1Ba2Cu3O7*. 1991: United States. p. 18p.

50. Schwarz, R.B. and C.C. Koch, *Formation of amorphous alloys by the mechanical alloying of crystalline powders of pure metals and powders of intermetallics.* Applied Physics Letters, 1986. **49**(3): p. 146-8.
51. Eckert, J., et al., *Glass-forming range in mechanically alloyed Ni-Zr and the influence of the milling intensity.* Journal of Applied Physics, 1988. **64**(6): p. 3224-8.
52. Hellstern, E. and L. Schultz, *Glass formation in mechanically alloyed transition-metal-Zr alloys.* Philosophical Magazine B (Physics of Condensed Matter, Electronic, Optical and Magnetic Properties), 1987. **56**(4): p. 443-8.
53. Sun, D.-Z., et al., *Calorimetry study of Ni50Ti50 ball milled powders.* Journal of Alloys and Compounds, 1992. **186**(1): p. 33-35.
54. Thompson, J.R., C. Politis, and Y.C. Kim. *Formation of powdered Hf-Ni, Hf-Cu and Hf-Ru materials by mechanical alloying methods*. 1988. Montreal, Que., Canada.
55. Goldwasser, D.J. and B.H. Kear. *Properties of a resin matrix composite reinforced with amorphous metal ribbons*. 1976. Cambridge, MA, USA.
56. Cytron, S.J., *A metallic glass-metal matrix composite.* Journal of Materials Science Letters, 1982. **1**(5): p. 211-13.
57. Blank-Bewersdorff, M., U. Koster, and G. Steinbrink, *Interfaces with improved adhesion in metal matrix/metallic glass composites.* Journal of Materials Science Letters, 1989. **8**(7): p. 796-8.
58. Zhang, Z., et al., *Synthesis of nanocrystalline aluminum matrix composites reinforced with in situ devitrified Al-Ni-La amorphous particles.* Scripta Materialia, 2006. **54**(5): p. 869-874.
59. Nagarathnam, K., et al. *Materials behavior and manufacturing aspects of high pressure combustion driven compaction P/M components*. 2004. Chicago, IL, USA: Metal Powder Industries Federation.
60. Sachan, M. and S.A. Majetich. *Combustion-driven compaction of nanostructured Sm-Co and Fe mixtures*. 2005. Nagoya, Japan: IEEE.
61. Yao, Y., et al., *Electrodeposition and mechanical and corrosion resistance properties of Ni-W/SiC nanocomposite coatings.* Materials Letters, 2007. **61**(1): p. 67-70.
62. Donten, M., H. Cesiulis, and Z. Stojek, *Electrodeposition and properties of Ni-W, Fe-W and Fe-Ni-W amorphous alloys. A comparative study.* Electrochimica Acta, 2000. **45**(20): p. 3389-3396.
63. Guo, Z., et al., *Electrodeposition of Ni-W amorphous alloy and Ni-W-SiC composite deposits.* Journal of Materials Science and Technology, 2000. **16**(3): p. 323-326.
64. Mukira, C.G. and T.H. Courtney, *Structure and Properties of Mechanically Alloyed and Consolidated Ni-W(Fe) Alloys*, in *Reprint: Structure and Properties of Mechanically Alloyed and Consolidated Ni-W(Fe) Alloys.* 1995: United States. p. 13p.
65. Betteridge, W., *Nickel and its Alloys*. 1977, Plymouth [England]: MacDonald and Evans, Ltd.
66. Farrar, J.C.M., *The alloy tree: A guide to low-alloy steels, stainless steels and nickel-base alloys*. 2004, Cambridge [England]: Woodhead Publishing, Ltd.

67. Erickson, G.L., *Polycrystalline cast superalloys*, in *in ASM Handbooks online*. 2002, ASM International.
68. Courtney, T.H., *Mechanical Behavior of Materials*. 1990, New York: McGraw-Hill.
69. Reed-Hill, R.E. and R. Abbaschian, *Physical Metallurgy Principles*. 3rd ed. 1994, Boston: PWS Pubishing.
70. Scattergood, R.O., et al., *Strengthening mechanisms in nanocrystalline alloys.* Materials Science and Engineering: A, 2008. **493**(1-2): p. 3-11.

Appendix A: Image Analysis

Particle size image analysis
Curves: shift white point input to 40
Curves: shift black point input to 60
Histogram: count below Level 100

1 hr attritor-blended powder			
pixels	particles	px/p	avg. diameter (μm)
255982	97	2638.99	58.0
238053	97	2454.155	55.9
284283	75	3790.44	69.5
108394	67	1617.821	45.4

3 hr attritor-blended powder			
pixels	particles	px/p	avg. diameter (μm)
679706	33	20597.15	161.9
3437668	52	66109	290.1
3183681	46	69210.46	296.9
1650100	34	48532.35	248.6

For the powder that was blended for one hour, the mean particle diameter is 57.2μm, and the standard deviation of the mean (not of an individual particle) is 9.9μm.

For the powder that was blended for three hours, the mean particle diameter is 249.4μm, and the standard deviation of the mean (not of an individual particle) is 62.1μm.

Porosity image analysis
1000x
Curves: shift white point input to 80
Histogram: count below Level 100

1 hr attritor-blended samples			
HT (hours)	counts	pixels	Por. %
10	1416	226304	0.63%
30	1584	226304	0.70%
50	1582	226304	0.70%

3 hr attritor-blended samples			
HT (hours)	counts	pixels	Por. %
10	446	226304	0.20%
30	492	226304	0.22%
50	575	226304	0.25%

Intermetallic volume %
400x
Histogram (1 hr): count Level 106–255
Histogram (3 hr): count Level 155–255

1 hr attritor-blended samples			
HT (hours)	counts	pixels	vol. %
10	20997	226304	9.28%
30	17299	226304	7.64%
50	17087	226304	7.55%

3 hr attritor-blended samples			
HT (hours)	counts	pixels	vol. %
10	6776	226304	2.99%
30	1260	226304	0.56%
50	850	226304	0.38%

Appendix B: Vickers macrohardness data

	Vickers macrohardness measurements									
	(attritor blending time [hours], sintering time [hours])									
	1, 5	**1, 10**	**1, 20**	**1, 30**	**1, 50**	**3, 5**	**3, 10**	**3, 20**	**3, 30**	**3, 50**
1	109.6	117.0	113.9	106.6	103.0	116.0	95.9	149.2	121.2	117.8
2	105.1	111.9	114.0	118.4	88.3	119.2	113.4	112.0	122.6	130.5
3	106.0	112.6	118.5	116.4	106.6	135.5	119.8	120.1	119.3	101.9
4	113.9	111.6	125.1	124.4	108.6	115.0	114.7	117.5	127.2	135.4
5	116.5	112.0	116.6	117.3	111.7	118.4	117.9	111.5	103.7	127.2
mean	110.2	113.0	117.6	116.6	103.6	120.8	112.3	122.1	118.8	122.6
std. dev.	4.9	2.3	4.6	6.4	9.1	8.4	9.5	15.6	8.9	13.2

Appendix C: EDS data

1 hour attritor milled, 10 hours sintering

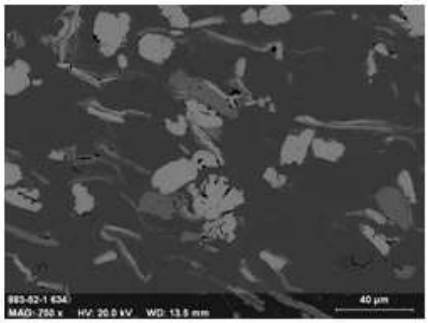

883-52-1 634Date:19/08/2008 11:18:22Image size:1000 x 750Mag:750xHV:20.0kV

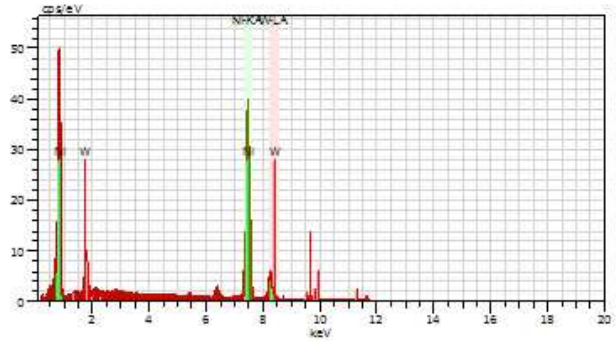

Puls th.:34.60kcps

Map data 286Date:19/08/2008 11:18:38Image size:1000 x 750Mag:750xHV:20.0kV

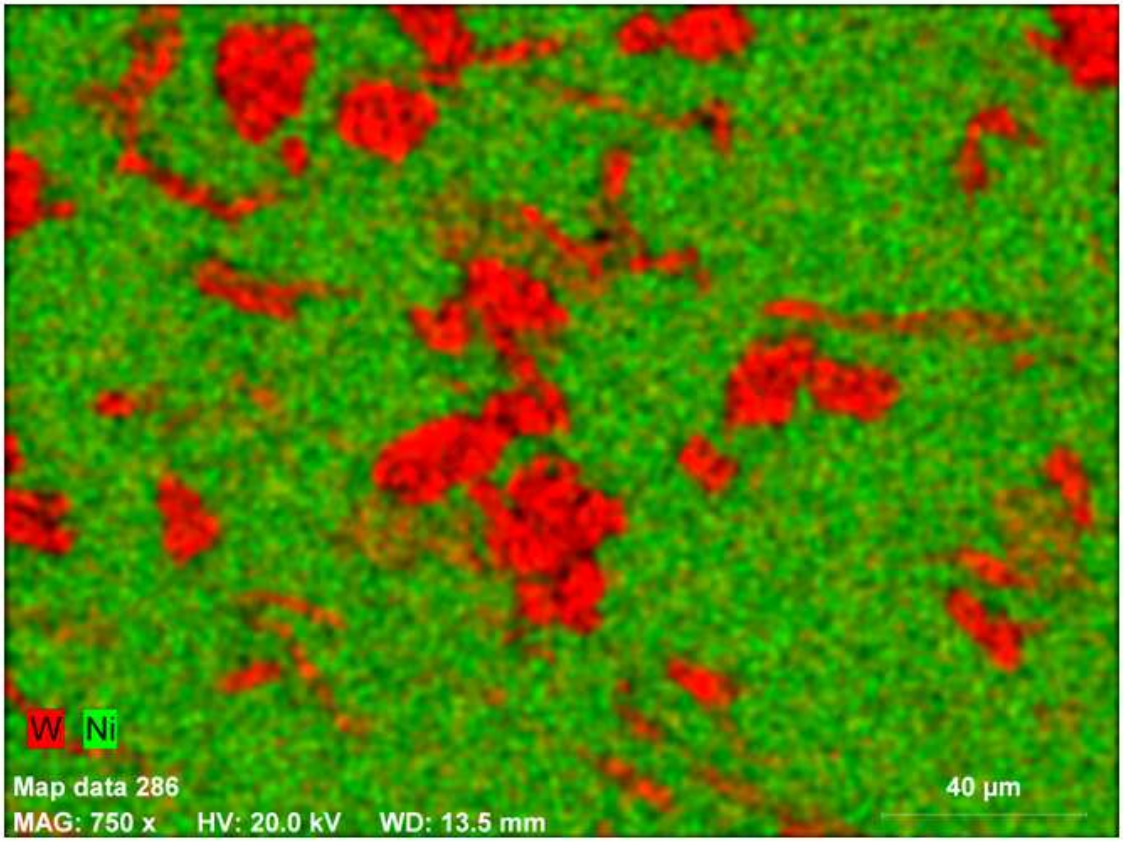

1 hour attritor milled, 50 hours sintering

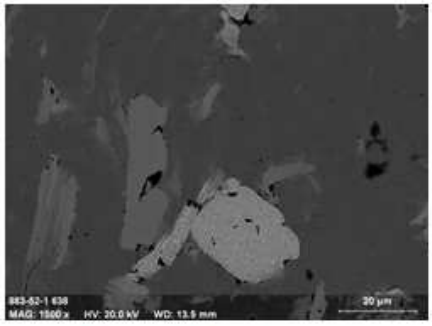

883-52-1 638Date:19/08/2008 11:54:38Image size:1000 x 750Mag:1500xHV:20.0kV

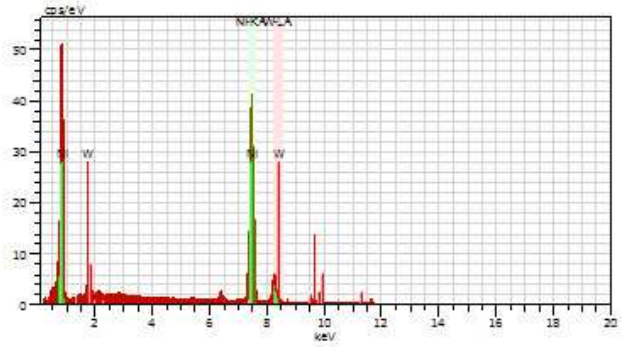

Puls th.:34.35kcps

Map data 287Date:19/08/2008 11:54:54Image size:1000 x 750Mag:1500xHV:20.0kV

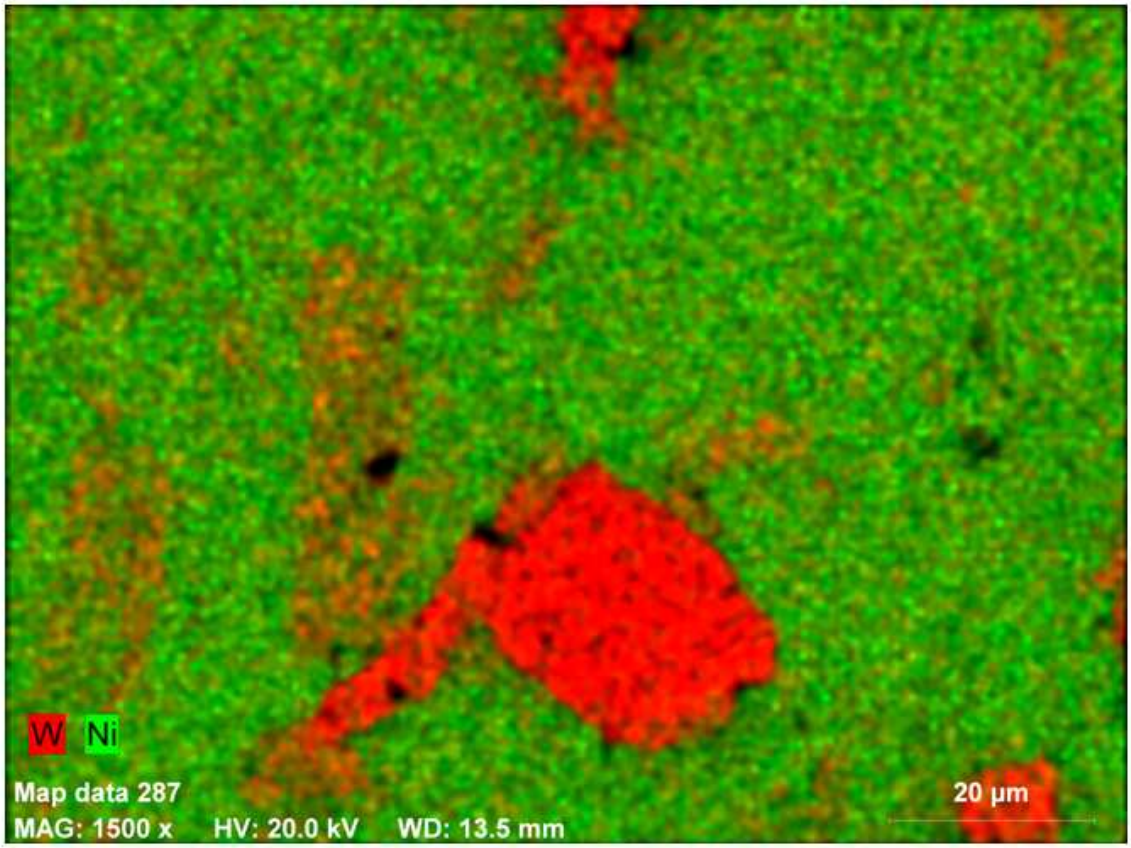

3 hours attritor milled, 10 hours sintering

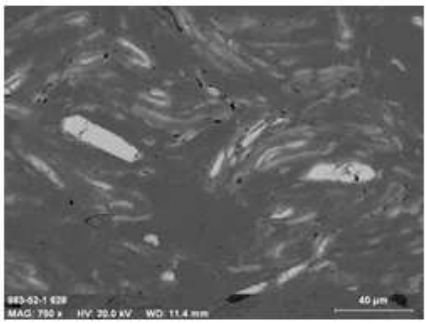

883-52-1 628Date:19/08/2008 10:14:03Image size:1000 x 750Mag:750xHV:20.0kV

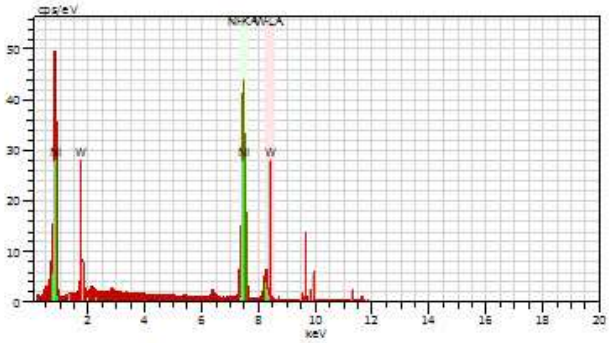

Puls th.:35.47kcps

Map data 284Date:19/08/2008 10:14:25Image size:1000 x 750Mag:750xHV:20.0kV

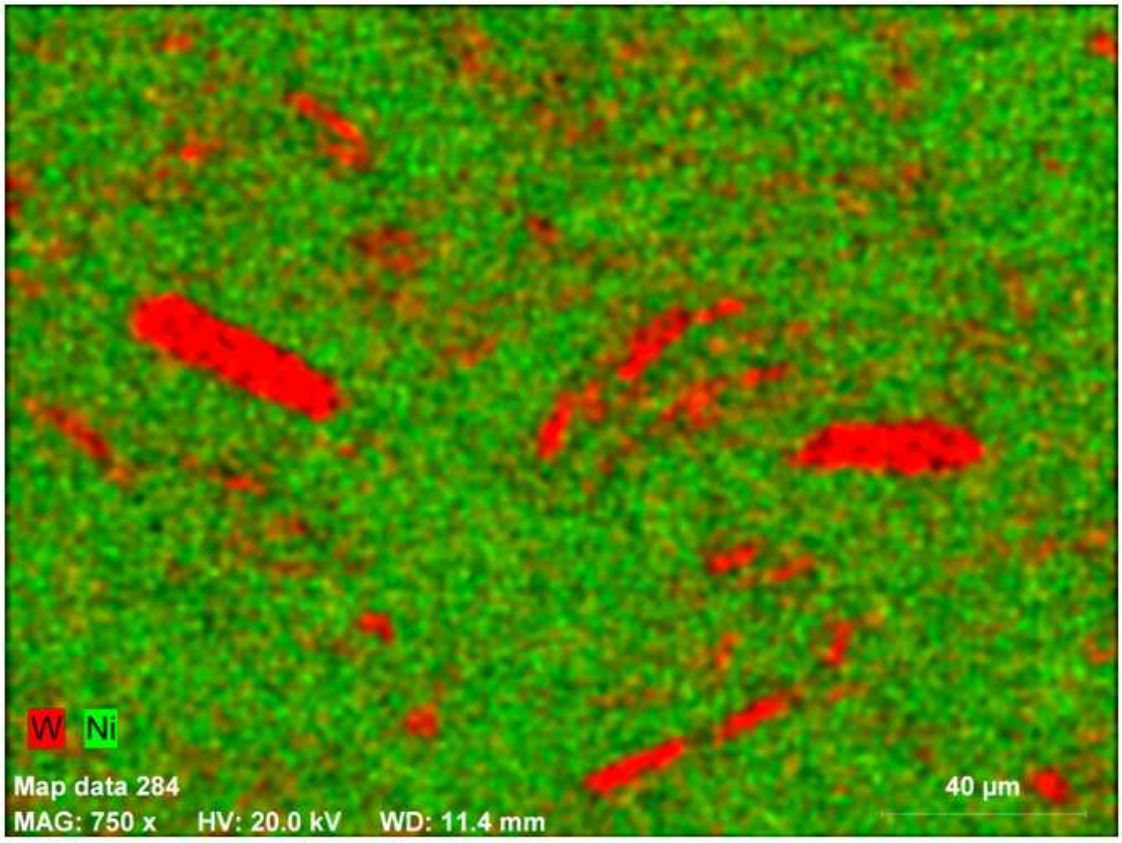

3 hours attritor milled, 50 hours sintering

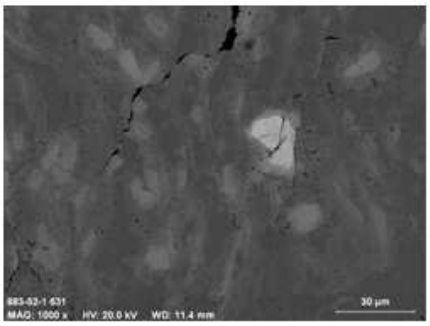

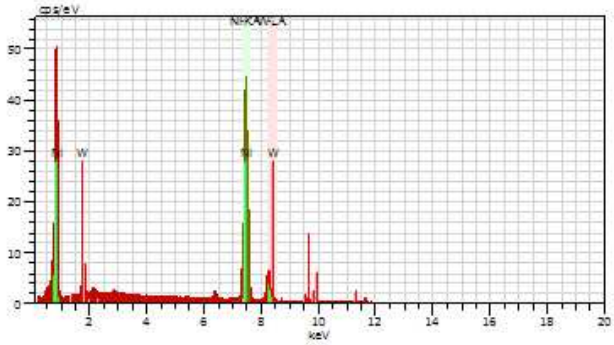

883-52-1 631Date:19/08/2008 10:54:50Image size:1000 x 750Mag:1000xHV:20.0kV

Puls th.:35.15kcps

Map data 285Date:19/08/2008 10:55:12Image size:1000 x 750Mag:1000xHV:20.0kV

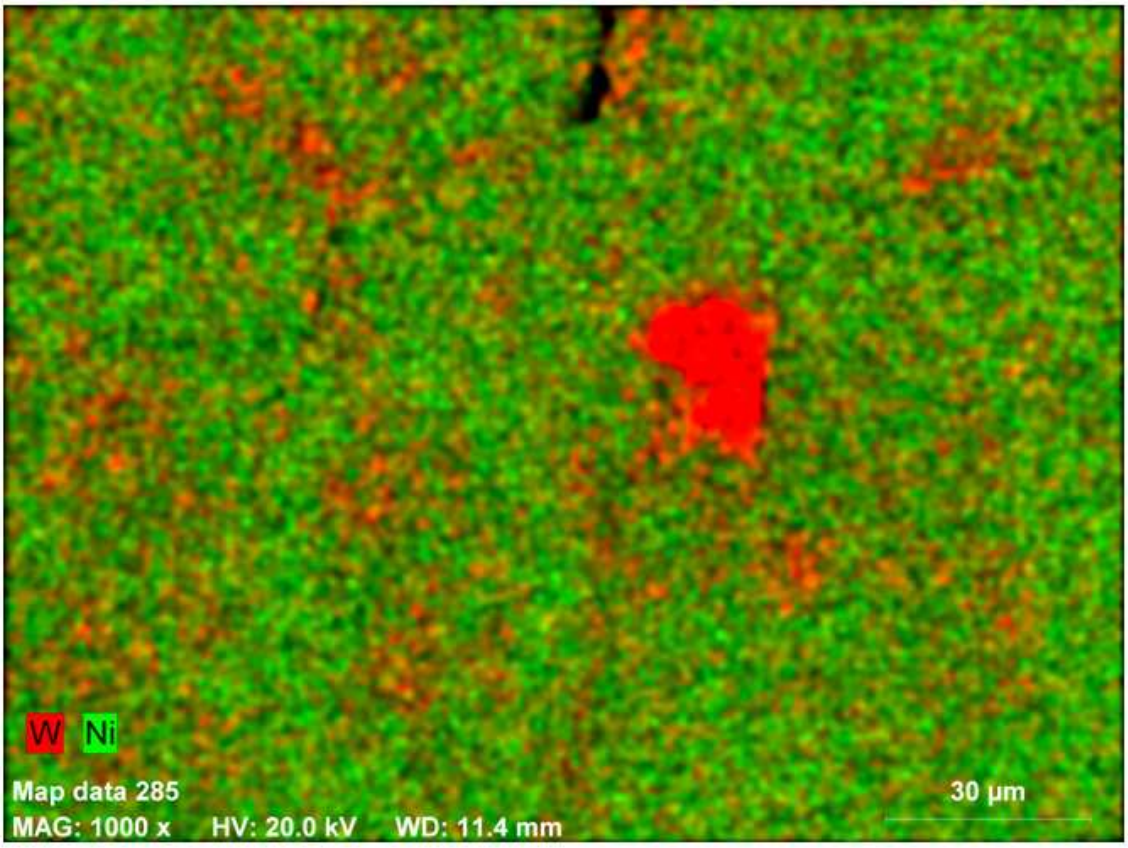

Local EDS analysis

1 hr attritor mill, 30 hr sinter

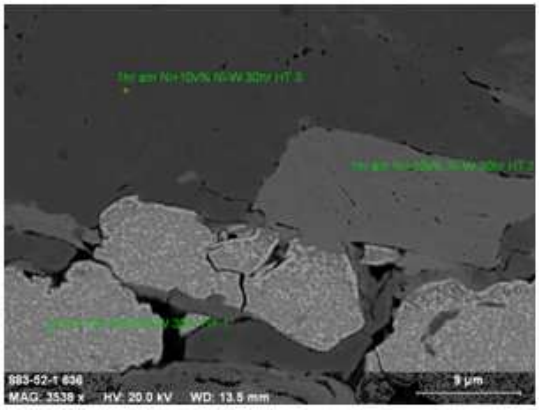

883-52-1 636Date:19/08/2008 11:29:37Image size:1000 x 750Mag:3538.00068733695xHV:20.0kV

1 hr attritor mill, 50 hr sinter

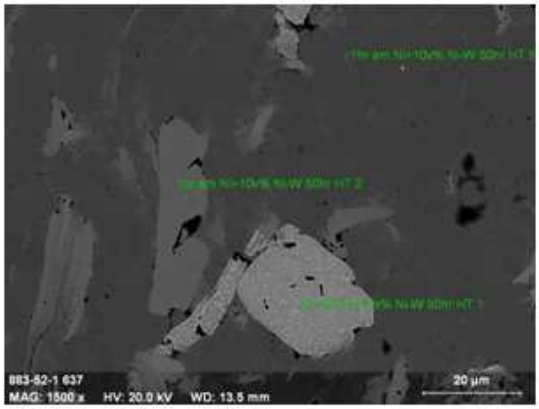

883-52-1 637Date:19/08/2008 11:47:09Image size:1000 x 750Mag:1500xHV:20.0kV

3 hr attritor mill, 30 hr sinter

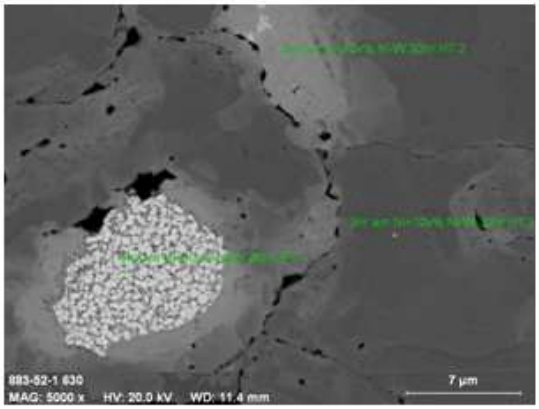

883-52-1 630Date:19/08/2008 10:37:05Image size:1000 x 750Mag:5000.00000000001xHV:20.0kV

3 hr attritor mill, 50 hr sinter

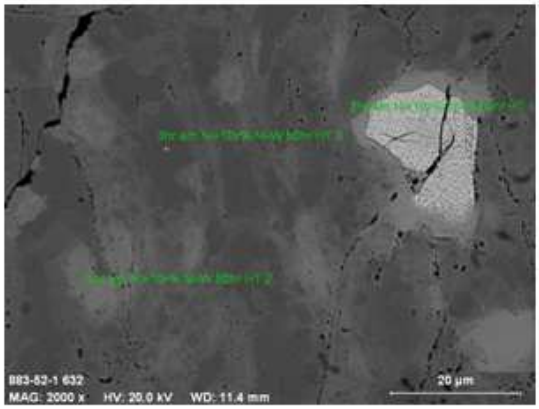

883-52-1 632Date:19/08/2008 11:00:34Image size:1000 x 750Mag:2000xHV:20.0kV

Point 1 corresponds to amorphous particle, point 2 corresponds to intermediate area, point 3 corresponds to nickel-rich matrix.

Normalized local EDS analysis

Point 1 local EDS analysis		
	W content	Ni content
1 hr, 30 hr	35.37%	64.63%
1 hr, 50 hr	31.05%	68.95%
3 hr, 30 hr	31.47%	68.53%
3 hr, 50 hr	40.35%	59.65%

Point 2 local EDS analysis		
	W content	Ni content
1 hr, 30 hr	11.02%	88.98%
1 hr, 50 hr	7.45%	92.55%
3 hr, 30 hr	13.32%	86.68%
3 hr, 50 hr	8.97%	91.03%

Point 3 local EDS analysis		
	W content	Ni content
1 hr, 30 hr	0.95%	99.05%
1 hr, 50 hr	0.88%	99.12%
3 hr, 30 hr	0.84%	99.16%
3 hr, 50 hr	0.90%	99.10%

The sample area in local EDS analysis is approximately $1\mu m^2$, therefore the composition of the tungsten-rich sub-particles must be backed out using a couple of assumptions:

1. The sub-particles constitute 75% of the reinforcement particle volume
2. The composition of the reinforcement particle matrix is equal to that of Point 2

Composition of Point 1 in 3 hr, 50 hr sample			
	Vol. %	W content	Overall W content
Matrix	25%	8.97%	40.35%
Sub-particle	75%	*50.81%*	